JGR Space Physics

RESEARCH ARTICLE
10.1029/2024JA033192

Total Electron Content Variations During an HSS/SIR-Driven Geomagnetic Storm at High and Mid Latitudes

G. P. Geethakumari[1], A. T. Aikio[1], L. Cai[1], H. Vanhamäki[1], I. I. Virtanen[1], A. Coster[2], A. Marchaudon[3], P.-L. Blelly[3], A. Maute[4,5], J. Norberg[6], S. Oyama[7,8], Y. Zhang[9], and B. S. R. Kunduri[10]

[1]Space Physics and Astronomy Research Unit, University of Oulu, Oulu, Finland, [2]Haystack Observatory, Massachusetts Institute of Technology, Westford, MA, USA, [3]IRAP, Université de Toulouse, CNRS, CNES, Toulouse, France, [4]Cooperative Institute for Research in Environmental Sciences, University of Colorado Boulder, Boulder, CO, USA, [5]NOAA Space Weather Prediction Center, Boulder, CO, USA, [6]Finnish Meteorological Institute, Helsinki, Finland, [7]ISEE, Nagoya University, Nagoya, Japan, [8]National Institute of Polar Research, Tachikawa, Japan, [9]The John Hopkins University Applied Physics Laboratory, Laurel, MD, USA, [10]Bradley Department of Electrical and Computer Engineering, Virginia Tech, Blacksburg, VA, USA

Key Points:

- High speed stream/SIR-driven moderate storm drives 6 days long depletion in total electron content (TEC) reaching at least 25% during each day from polar to mid latitudes
- Mid-latitude TEC depletions in late morning correlate spatially with regions of increased $\Sigma O/N_2$ as measured by TIMED/Global Ultra Violet Imager
- In the nightside auroral oval TEC increases reaching 6 TECU (200%) and shows temporal correlation with the Auroral electrojet index

Supporting Information:

Supporting Information may be found in the online version of this article.

Correspondence to:

G. P. Geethakumari,
gopika.prasannakumara@oulu.fi

Citation:

Geethakumari, G. P., Aikio, A. T., Cai, L., Vanhamäki, H., Virtanen, I. I., Coster, A., et al. (2024). Total electron content variations during an HSS/SIR-driven geomagnetic storm at high and mid latitudes. *Journal of Geophysical Research: Space Physics*, *129*, e2024JA033192. https://doi.org/10.1029/2024JA033192

Received 19 AUG 2024
Accepted 15 NOV 2024

Abstract Two interacting high-speed solar wind streams (HSSs) and associated stream interaction regions (SIR) caused a moderate geomagnetic storm during 14–20 March 2016. The spatio-temporal evolution of the total electron content (TEC) during the storm is studied by using Global Navigation Satellite System (GNSS) data. The moderate storm caused significant and long-lasting changes on TEC within the polar cap (70°–90° MLAT), at auroral and sub-auroral latitudes (60°–70° MLAT), and at mid-latitudes (40°–60° MLAT). A 25%–50% depletion in TEC was observed for six days in the day, dusk and dawn sectors in the polar cap region and in the day and dusk sectors at the auroral and sub-auroral latitudes. Sub-auroral polarization streams observed by the Defense Meteorological Satellite Program satellite contributed to the sub-auroral dusk TEC decreases. At mid-latitudes, TEC depletion was observed in all local time sectors 21 hr after the storm onset. It is suggested that ion-neutral frictional heating causes the TEC depletions, which is further supported by the observed spatial correlation between TEC depletions and $\sum O/N_2$ decreases at mid-latitudes observed by TIMED/GUVI. The storm induced a prolonged positive phase at mid-latitudes lasting 9 hr. In the polar cap, enhancements of TEC up to 200% were caused by polar cap patches. TEC increases were the dominant feature in the night and morning sectors within the auroral oval because of particle precipitation and resulted up to regionally averaged 6 TECU (200%) increases.

Plain Language Summary Interaction of solar wind with the Earth's magnetosphere can cause perturbations to the geomagnetic field, known as geomagnetic storms. This study presents the ionospheric response to a moderate geomagnetic storm during 14–20 March 2016 caused by high-speed solar wind streams, characterized by its high velocity >500 km/s. Total electron content (TEC) maps from Global Navigation Satellite System were used to study the electron density variations during the storm. With the commencement of the storm, a 25%–50% decrease in TEC was observed on the dayside, duskside and dawn side in the polar cap region. In the auroral and sub-auroral region, the storm caused a depletion on the dayside and duskside. Strong auroral precipitation during the storm caused a 200% increase in TEC in the night side auroral oval. The initial response at mid latitudes was a long duration enhancement in TEC that lasted for 9 hr followed by a decrease in TEC that persisted till 20 March. The TEC depletion at mid latitudes shows spatial correlation with neutral composition changes agreeing with previous studies. The composition change originates from high latitudes, where the atmosphere is heated because of strong electric fields.

1. Introduction

The large-scale disturbances in the solar wind affect the coupling with the magnetosphere and can cause severe impacts on the terrestrial ionosphere. During the declining phase of the solar cycle, solar wind high speed streams (HSSs) emanate from coronal holes (Krieger et al., 1973; Phillips et al., 1995; Sheeley et al., 1976) with speeds ranging from 500 to 800 km/s and lasting for at least two days (Grandin et al., 2019; Kavanagh et al., 2012). HSSs catch up with the previously emitted slow solar wind (300–400 km/s) and form a compressed region in the interplanetary medium called co-rotating interaction region (CIR) or stream interaction region (SIR) (Belcher & Davis, 1971; Richardson, 2018; Smith & Wolfe, 1976). In this study, we use the latter term. Coronal holes can

persist for several solar rotations, causing a periodicity of 27 days in the solar wind and resulting in recurring geomagnetic activity (Crowley et al., 2008; Tsurutani et al., 1995).

It is known that when an HSS with a SIR interacts with the magnetosphere, typically a weak (Dst > -50 nT) to moderate ($-100 <$ Dst ≤ -50 nT) geomagnetic storm is produced (Denton et al., 2006; Gonzalez et al., 1994; Lakhina & Tsurutani, 2016; Tsurutani et al., 2006). Geomagnetic storms deposit large amounts of energy into the magnetosphere–ionosphere–thermosphere system causing large scale variations in the ionospheric electron density, typically referred to as ionospheric storms (Buonsanto, 1999; Prölss, 1980). Ionospheric storms are manifested either as an increase or decrease in TEC, referred to as positive or negative storm phases, respectively (Prölss, 1997). Geomagnetic storms and the related ionospheric storms have been extensively studied for decades, but the focus has been on intense geomagnetic storms, typically caused by coronal mass ejections (CMEs). Though some studies have been made on the HSS/SIR driven storm impacts on ionospheric parameters and neutral composition in the mid and low latitudes (e.g., Buresova et al., 2014; Denton et al., 2009; Lei et al., 2011; Verkhoglyadova et al., 2013; Wang et al., 2011), and on a global scale (e.g., Burns et al., 2012; Tulasi Ram et al., 2010), very few studies have focused on the response of the high latitude ionosphere.

Grandin et al. (2015) studied the changes in ionospheric parameters using the high-latitude Sodankylä ionosonde during HSS/CIR events in 2006–2008. They found that the F-layer critical frequency foF2, which is proportional to the square root of peak electron density, was decreased in the 12–23 magnetic local time (MLT) sector for several days. The strongest depletion occurred during equinoxes. The proposed driver was ion–neutral frictional heating at high latitudes, discussed also in Marchaudon et al. (2018). A short-lived foF2 increase was visible during all seasons near noon on the first day after the arrival of the HSS/CIR and several days long enhancement in the morning sector during equinoxes and in winter. These enhancements were attributed to particle precipitation effects.

As the geomagnetic storms perturb the ionosphere, the neutral atmosphere (thermosphere) is also affected. During HSS/SIR driven storms the magnetosphere convection driven by solar wind interaction with magnetosphere is enhanced, which leads to increase in the cross polar cap potential (CPCP) (e.g., Heelis & Sojka, 2011) and in the Joule heating rate at high latitudes. This can effectively cause mass density (Lei et al., 2008; Thayer et al., 2008) and composition variations in the thermosphere as observed in the $\sum O/N_2$ measurements (Crowley et al., 2008; Zhang & Paxton, 2021; Zhang et al., 2004). Various studies have already shown that depletions of $\sum O/N_2$ during geomagnetically active periods can potentially cause negative ionospheric storms (Fuller-Rowell et al., 1994; Zhang & Paxton, 2021).

In this paper, we will characterize the ionospheric response to a long-lasting HSS/SIR driven moderate geomagnetic storm between 40° and 90° magnetic latitudes (MLAT) in the northern hemisphere, using the Global Navigation Satellite System (GNSS) TEC data together with a comprehensive set of other measurements. The aim is to study the time evolution of TEC separately within the polar cap, at auroral and sub-auroral latitudes, and at mid-latitudes and cast light on the processes that cause decreases and increases in TEC at these regions within day, dusk, night and dawn sectors. The TEC measurements are put in the context of global plasma convection and field aligned currents (FACs) by using the SuperDARN radar and the AMPERE project data, respectively. We also use the Global Ultra Violet Imager (GUVI) instrument of the TIMED satellite to observe the neutral composition changes at mid-latitudes as characterized by $\sum O/N_2$.

The full data set and analysis methods used in this study are described in Section 2. Observed results are shown Section 3 and the plausible mechanisms are discussed in Section 4. Conclusions are presented in the final section.

2. Data and Analysis Methods

The GNSS TEC, which is the column integrated electron density between the GNSS satellite and the receiver, is analyzed during the storm event 14–21 March 2016. The Madrigal database provides TEC maps in the geographical coordinate system with a latitude-longitude resolution of 1° by 1° and a time resolution of 5 min. The TEC maps are derived based on the MIT Automated Processing GPS (MAPGPS) algorithm from dual frequency data of over 140 GNSS satellites (Rideout & Coster, 2006; Vierinen et al., 2016). We have projected the TEC maps from the geographic coordinate system to the Altitude-Adjusted Corrected Geomagnetic Coordinate System (AACGM) (Shepherd, 2014) with the help of GeoSpaceLab (Cai et al., 2022).

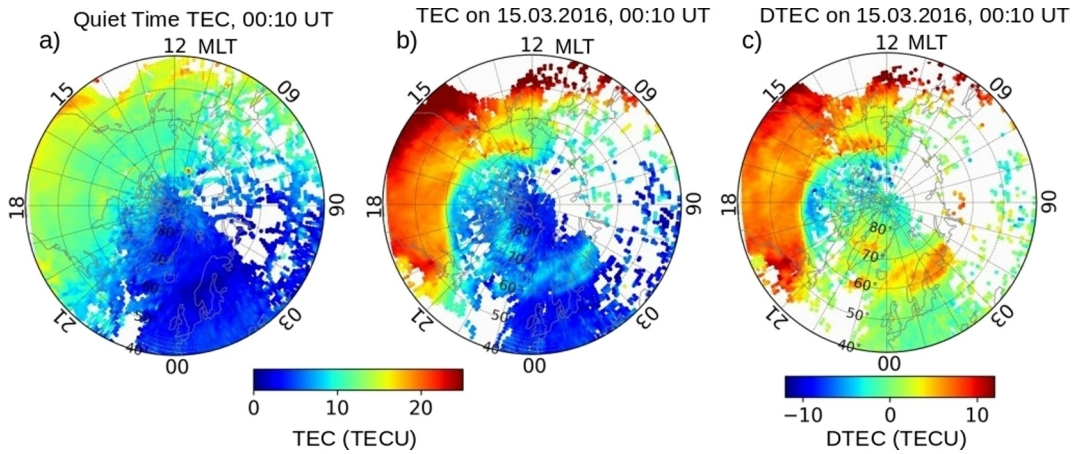

Figure 1. Example of calculation of DTEC: (a) Background total electron content (TEC), (b) Observed TEC on 15.03.2016 at 00:10 UT, (c) DTEC after subtracting background TEC from the observed TEC. The TEC maps are presented in AACGM MLT-MLAT coordinate system.

To reduce the spatial data gaps, 20-min averages of the TEC maps are calculated. As the time window for averaging is extended, more satellite-receiver pairs are identified, resulting in a greater number of data points. Because we are interested in seeing the changes in TEC produced by the storm, the quiet-time background is subtracted from the 20-min average TEC maps, and the result is called DTEC in this study. The quiet-time background is determined by averaging the TEC maps during the four quietest days of the month, which were March 5, 13, 25 and 26. The mean Kp index during those days was 1^- and the Kp index maximum was 1^+. The previous storm before the storm during 14–20 March reached the SYM-H minimum on 6 March and was recovered by 11 March. The background is calculated for each 20-min time interval during 24 hr, corresponding to one rotation of the Earth.

An example is shown in Figure 1 on 15 March 2016 at 00:10 UT. Figures 1a and 1b show the quiet time background TEC and the measured TEC map at 00:10 UT (average over 00:00–00:20 UT), respectively. Figure 1c shows the DTEC map, which is obtained by subtracting the background TEC in Figure 1a from the measurement in Figure 1b. Positive DTEC values indicate enhancements in TEC and negative values indicate depletions. The unit is TEC Unit (TECU), where 1 TECU = 10^{16} electrons/m^2. The mean error in individual 1° x 1° bins during the event at 70–90° MLAT is 0.95 TECU, at 60–70° MLAT 0.64 TECU and at 40–60° MLAT 0.49 TECU.

The Active Magnetosphere and Planetary Electrodynamics Response Experiment (AMPERE) project provides FAC maps every 10 min during this event. AMPERE is a constellation of 66 satellites having six polar orbital planes, each circling the Earth at an altitude of 760 km. The FAC maps are derived from the magnetic field perturbations measured by the onboard magnetometers (Anderson et al., 2000, 2014; Coxon et al., 2018). The Super Dual Auroral Radar Network (SuperDARN) of coherent scatter radars at high latitudes in the Northern and Southern hemispheres measure the line-of-sight plasma velocities in the F-region (Chisham et al., 2007; Ruohoniemi & Baker, 1998). Based on the measurements and a statistical model, the ionospheric electric potential maps are derived (Ruohoniemi & Baker, 1998; Thomas & Shepherd, 2018) and used in this study. Both the AMPERE and SuperDARN data provide a global view of the high-latitude electrodynamics affected by the solar wind–magnetosphere coupling during the storm.

For thermospheric composition, we used the ratio of column-integrated atomic oxygen number density O to molecular nitrogen number density N_2, denoted as $\sum O/N_2$, obtained using the dayglow imager GUVI measurements onboard the Thermosphere Ionosphere Mesosphere Energetics and Dynamics Mission (TIMED) satellite (Christensen et al., 2003). The TIMED satellite has an orbital inclination of 74.1° and it encircles the Earth in 97.3 minutes. During this event, the satellite's ascending and descending times were 20–22 local solar time (LST) on the nightside and around 8–10 LST on the dayside, respectively. Hence, GUVI provided the $\sum O/N_2$ ratio data in the pre–noon sector for this event.

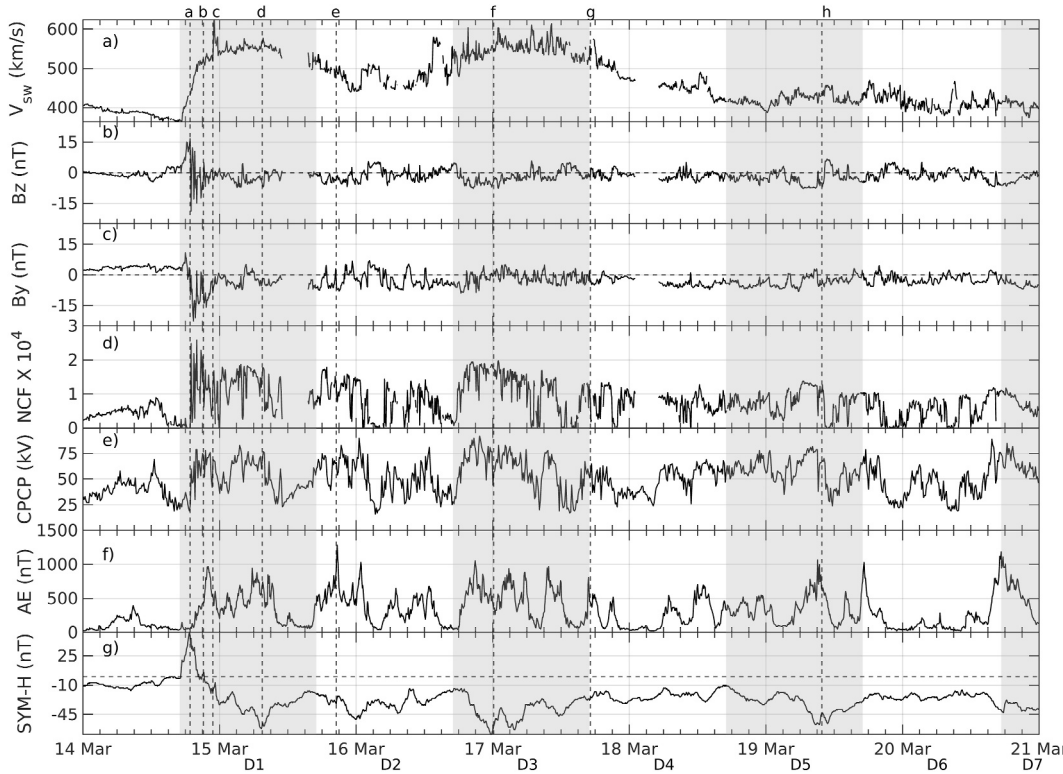

Figure 2. Solar wind parameters and geomagnetic variations for 14–20 March 2016. (a) Solar wind speed, (b) interplanetary magnetic field (IMF) B_z and (c) IMF B_y in Geocentric Solar Magnetospheric coordinate system, (d) Newell coupling function, (e) cross polar cap potential, (f) Auroral electrojet index and (g) SYM-H index. The sequence of shaded and non-shaded periods indicate the days after the storm onset numbered D1–D7. The dashed vertical lines indicate the selected times shown in Figure 3.

The Defense Meteorological Satellite Program (DMSP) provides us with the cross-track ion velocities from the Special Sensor for Ions, Electrons, and Scintillation (Rich & Hairston, 1994) and auroral images are obtained from the Special Sensor Ultraviolet Spectrographic Imagers (SSUSI, Paxton et al., 2002).

Data for the solar wind, interplanetary magnetic field (IMF) and geomagnetic indices were taken from the OMNI database (King & Papitashvili, 2005) with a cadence of 5 min. In this study,the SYM-H index, a high resolution version of Dst index with a temporal resolution of 1 min (Wanliss & Showalter, 2006) is used.

3. Observations and Results

3.1. Solar Wind and Storm Development

Figure 2 shows the solar wind conditions and the geomagnetic disturbance from 14 to 20 March 2016. As can be seen in Figure 2a, the solar wind speed starts to rise from 380 km/s on 14 March at 17:25 UT and reaches 624 km/s on 14 March at 23:05 UT, after which it gradually decreases, though it does not fully recover, reaching a local minimum on 16 March. After 12:25 UT on 16 March, it again shows a gradual increase with the peak on 17 March.

Solar wind speeds exceeding 500 km/s are often used as one of the criteria to identify HSS (Grandin et al., 2019; Kavanagh et al., 2012). Both of the solar wind peak velocities exceed this threshold, suggesting that the event is caused by two interacting HSSs. Indeed, three to four days before March 14, the Sun hosted several extended and long-lived coronal holes, which are known to be the sources of solar wind HSSs (Krieger et al., 1973; Richardson, 2018; Sheeley et al., 1976).

Figures 2b and 2c show the B_z and B_y components in the Geocentric Solar Magnetospheric (GSM) coordinate system respectively. When the first HSS hits the magnetosphere on 14 March, IMF B_z component is first positive

(northward) until 18:50 UT. The B_y component remains negative for about 2 hr until 20:00 UT. Meanwhile, B_z rapidly fluctuates between 20 nT and −25 nT. During the later days of the storm, B_z and B_y components show fluctuations with amplitudes smaller than 10 nT. A part of those fluctuations are likely to be Alfvénic fluctuations that are observed within HSSs (Tsurutani et al., 2020, & references therein).

Figure 2d shows the Newell coupling function (NCF; Newell et al., 2006), which is used to estimate the strength of solar wind-magnetosphere coupling. The NCF depends on the solar wind speed, magnitude of the transverse magnetic field and the clock angle defined by the IMF B_z and B_y components. The NCF starts to increase when B_z turns southward on 14 March at 18:50 UT and reaches a peak value at 20:00 UT. After that, the NCF stays high (above 10,000) on 15 March, though fluctuating and the second peak is observed on 17 March at 00:55 UT during the second HSS. Increases of the southward component of the IMF produce the enhancements in NCF.

Figure 2e shows the SuperDARN cross polar cap potential (CPCP) (Ruohoniemi & Baker, 1998), which is the difference between the maximum electrostatic potential in the dawn cell and the minimum potential in the dusk cell of the ionosphere. The CPCP value and the size of the polar cap depend mainly on the solar wind velocity and the IMF parameters, and they together determine the average plasma convection speed in the polar cap. Comparing Figures 2d and 2e, the temporal variation of NCF and CPCP looks similar, despite the fact that SuperDARN CPCP values relies on statistical model when measurements are scarce. Similar to NCF, CPCP starts to increase at 18:50 UT on 14 March with the southward turning of B_z. On 16 March 21:40 UT, CPCP reaches a peak value of 92 kV with a daily maximum reaching 75 kV, except on D4 and D6.

Auroral electrojet (AE) index (Davis & Sugiura, 1966), shown in Figure 2f, starts to rise during the storm sudden commencement (SSC) peak at 18:45 UT suggesting substorm onset. A series of substorms is observed during the entire storm event. Note the good correlation between the NCF and the AE index, specifically during the first 3 days of the storm.

Figure 2g displays the SYM-H index. The first HSS reached the Earth's bow shock on 14 March at 17:20 UT, causing a positive excursion in the SYM-H index known as a SSC, which marks the initial phase of a geomagnetic storm and is caused by the increase of magnetopause current. The SYM-H index reaches a maximum of 50 nT at 18:45 UT and then slowly decreases during a total SSC duration of 3 hr. At 21:15 UT, SYM-H becomes negative, marking the main phase onset and intensification of the ring current. It reaches a minimum of −61 nT on 15 March at 07:20 UT and later recovers temporarily. On 15 March at 23:55 UT, SYM-H reaches a second minimum of about −50 nT. The SYM-H reached a third, double minimum, on 16 March at 23:40 UT and on 17 March at 03:50 UT with values −69 nT and −63 nT, respectively, and the fourth, double minimum of −60 nT takes place on 19 March at 08:55 UT and 10:50 UT, respectively. During the storm, the minimum Dst value is −56 nT. According to the classification of geomagnetic storms by Gonzalez et al. (1994), the range $-100\ \text{nT} < \text{Dst} \leq -50\ \text{nT}$ is considered a moderate geomagnetic storm. The SYM-H variations show that from 14 March to 20 March, a prolonged moderate geomagnetic storm with four minima below −50 nT occurred. The SYM-H recovered later on 21 March at 03:50 UT reaching −15 nT.

The 24-hr periods after the onset of the initial phase of the storm on 14 March at 17:20 UT are marked as Day 1 (D1), Day 2 (D2) …and Day 7 (D7) and they are shown on the bottom of the last panel in Figure 2.

Figure 3 gives an overview of the DTEC variations at different stages of the storm, with the times marked by the black vertical dashed lines with labels a–h in Figure 2. Below we will give a brief description and a more detailed discussion of the DTEC time variations at different latitudes will be provided in the next sections. Movies for each calendar day of the storm with 20-min resolution in the same format as Figure 3 are found in Movies S1–S7. In addition to movies of DTEC, movies of the original TEC are provided in the Movies S8–S14. In each panel of Figure 3, the left polar plot shows the DTEC as estimated by the method described in Section 2. Yellow-red colors indicate enhancement in TEC and blue indicate depletion. The right polar plot shows the FACs estimated by AMPERE, where the yellow-red colors show the upward FAC and blue the downward FAC. Overlaid on the polar plots are the contours of electric potential from SuperDARN. The equi-potential contours show the plasma convection streamlines in the F region ionosphere, as the plasma makes the $E \times B$ drift.

Figure 3a depicts the DTEC, potential contours, and FAC on 14 March at 19:10 UT during the SSC peak, when IMF B_z is still northward but B_y is fluctuating. During northward IMF B_z conditions, the CPCP is small and the FACs are concentrated on the dayside with a complicated structure of four current sheets. DTEC shows small

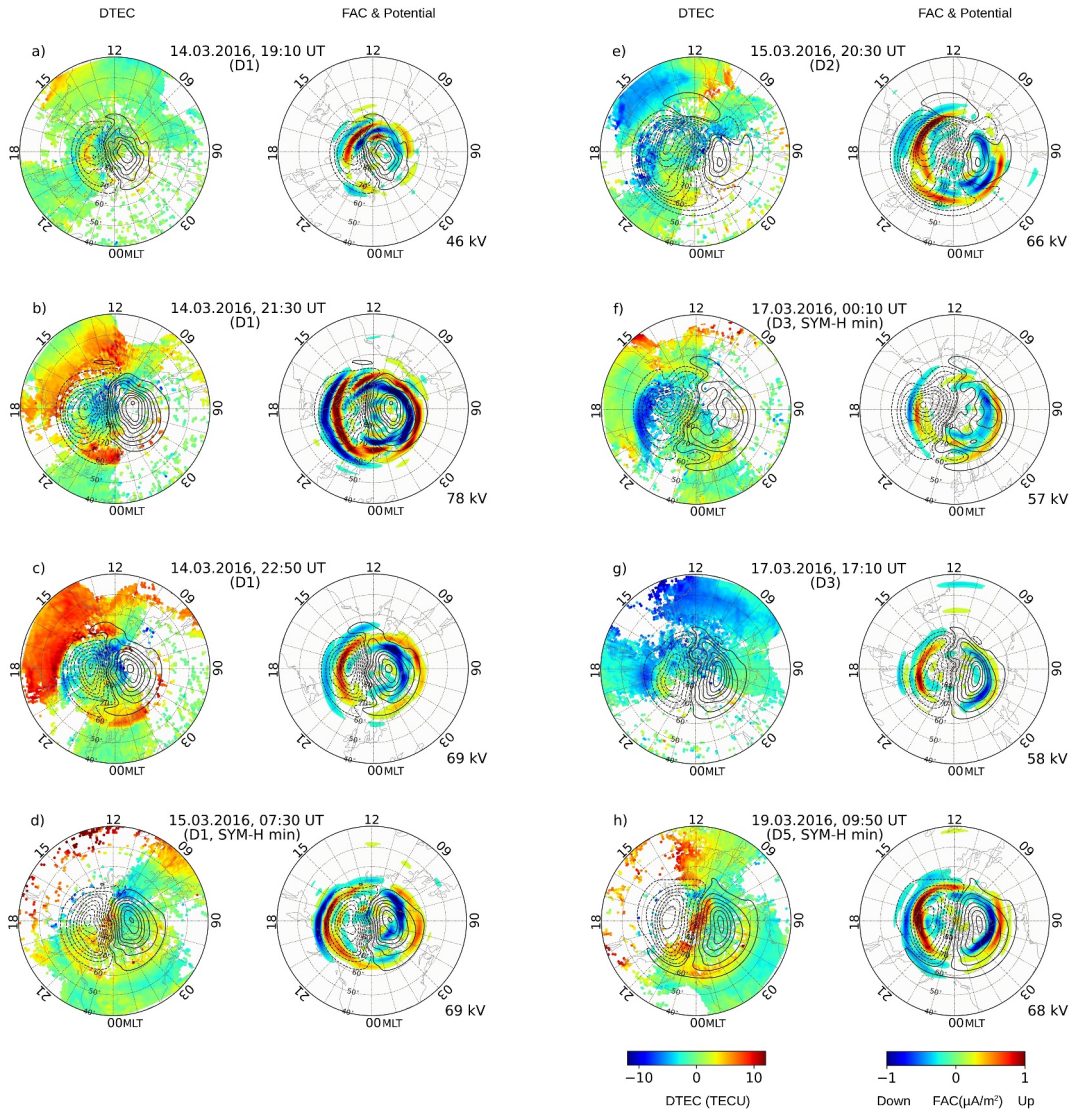

Figure 3. Panels a–h showing DTEC (difference between the measured TEC and the quiet background value of TEC) on the left side and AMPERE field aligned current on the right side, both presented in polar AACGM MLT-MLAT coordinate system, at instances corresponding to the dashed vertical lines in Figure 2. Occurrences of SYM-H minima are indicated in the panel title. Electrical equipotential contours are overlaid on both the panels with a step size of 5 kV and on the right bottom corner of each panel the cross polar cap potential from SuperDARN is given. The lowest latitude shown is 40° MLAT.

variations at high latitudes with a minor enhancement within the same region as the upward FAC, but no large-scale significant changes in DTEC can be observed.

Figure 3b at 21:30 UT corresponds to the time when SYM–H turns negative in the beginning of the main phase. The CPCP has increased to 78 kV and the convection pattern has expanded to lower latitudes. The FACs have intensified and show a pattern typical for the observed IMF B_y negative conditions (Anderson et al., 2008). The midnight sector shows three sheets of currents, typical for substorm conditions. DTEC enhancement is seen forming in the noon and dusk sectors at latitudes below the most equatorward plasma convection streamlines corresponding to the storm positive phase at mid– latitudes. A significant increase of DTEC in the nightside auroral oval is also observed during this time in association with the enhanced upward FAC and it is obviously associated with auroral precipitation. Meanwhile, a depletion in DTEC is seen in the polar cap.

Figure 3c is 80 min after panel b displaying the situation during the maximum of the mid-latitude positive phase. The strong enhancement in DTEC in the noon to dusk sector has extended to the lowest latitudes shown, that is, to 40° MLAT. Development of a storm time enhanced density (SED) plume (Foster, 1993; Foster et al., 2005), stretching from the dusk–side mid-latitudes toward the noon–time cusp at 12 MLT, is clearly visible in the figure. TEC enhancement due to strong auroral precipitation continues in the night side auroral oval. The deep depletion in DTEC prevails within the antisunward moving plasma in the polar cap and generally at high latitudes excluding the night sector. Another region of depleted DTEC occurs near 18 MLT just poleward of the strong enhancement. This region is embedded by the downward FAC.

The DTEC enhancements in the nightside auroral oval and at mid-latitudes remain only for some hours in the beginning of the main phase on D1. During the second half of D1, DTEC enhancements weaken as seen in the Movie S2 and discussed in Sections 3.3 and 3.4.

Figure 3d shows the DTEC and FAC on 15 March 07:30 UT during the latter part of D1, when the SYM-H index has reached its first local minimum. The main feature during this time is the enhancement of DTEC in the middle of polar cap, which is a polar cap patch (Carlson et al., 2004; Moen, Jøran et al., 2013; Weber et al., 1986) as discussed more detailed in Sections 3.2 and 4.2. The IMF B_z is southward and drives the relatively strong convection and FACs and the associated dayside reconnection could be producing the polar cap patches.

Figure 3e shows the DTEC variations on 15 March at 20:30 UT (D2), when the SYM-H index has increased after the first minimum on D1, but has not yet reached the second local minimum on D2. The AE index has a maximum value of 1,280 nT and the CPCP is 66 kV. At high latitudes (auroral oval and polar cap), the dominant feature is TEC depletion, though the effect of a polar cap patch on the nightside can be seen. At mid-latitudes, the positive phase has changed to a negative phase as DTEC shows a decrease from the noon to the dusk sector. Interestingly, on the west coast of the American sector, an enhancement in DTEC is seen.

Figure 3f shows 17 March at 00:10 UT (D3), close to the time of the third minimum in the SYM-H index, which is also the deepest minimum during the whole storm. During this time the second HSS has hit the magnetopause and the solar wind speed is high. The most significant feature is the latitudinally narrow depletion in DTEC in the dusk sector at the equatorward boundary of the convection pattern. This kind of feature was observed several times during the storm and it will be further discussed in Section 4.

In Figure 3g on 17 March at 17:10 UT (end of D3), the SYM-H index has recovered, but a strong depletion of DTEC is observed globally, particularly in the noon sector. The AE index reached 800 nT 20 min earlier and the CPCP is 58 kV.

Figure 3h shows the DTEC, potential and FAC during the fourth SYM-H minimum on 19 March 09:50 UT (D5) when the solar wind speed has decreased after the two HSSs. However, the southward IMF B_z has still kept the Newell coupling function values high during the previous hours and the AE index is high as well. A strong elongated polar patch as well as enhancements in the nightside and morning auroral oval are observed. Furthermore, a DTEC enhancement near noon at mid-latitudes is seen, but whether that would be continued to the afternoon and dusk sectors cannot be seen due to a lack of measurements in that sector.

3.2. Polar Cap TEC Variations

To obtain an overview of the complex latitude - local time variations in DTEC, we bin the data into three magnetic latitude ranges and four MLT sectors and calculate the average values of DTEC in those. The ranges are 70°– 90° MLAT corresponding roughly to the polar cap, 60°– 70° MLAT corresponding roughly to the auroral and sub-auroral latitudes, and 40°– 60° MLAT corresponding to the upper end of mid-latitudes. The local time sectors are 03–09 MLT (dawn), 09–15 MLT (dayside), 15–21 MLT (dusk) and 21-03 MLT (nightside). Since the number of GNSS receivers is small in certain geographical regions, average values are shown only for those points, where the number of data points is larger than 300. The TEC variations compared to the quiet time (DTEC) are presented in units of TECU in Figures 4–6. Calculating the error propagation for the data shown in those figures, we find that the mean values for DTEC error are 0.05 TECU in the polar cap, 0.04 TECU at auroral and sub-auroral latitudes and 0.02 TECU at mid-latitudes. The same DTEC variations are presented in percentages in Figures S1–S3 in Supporting Information S1.

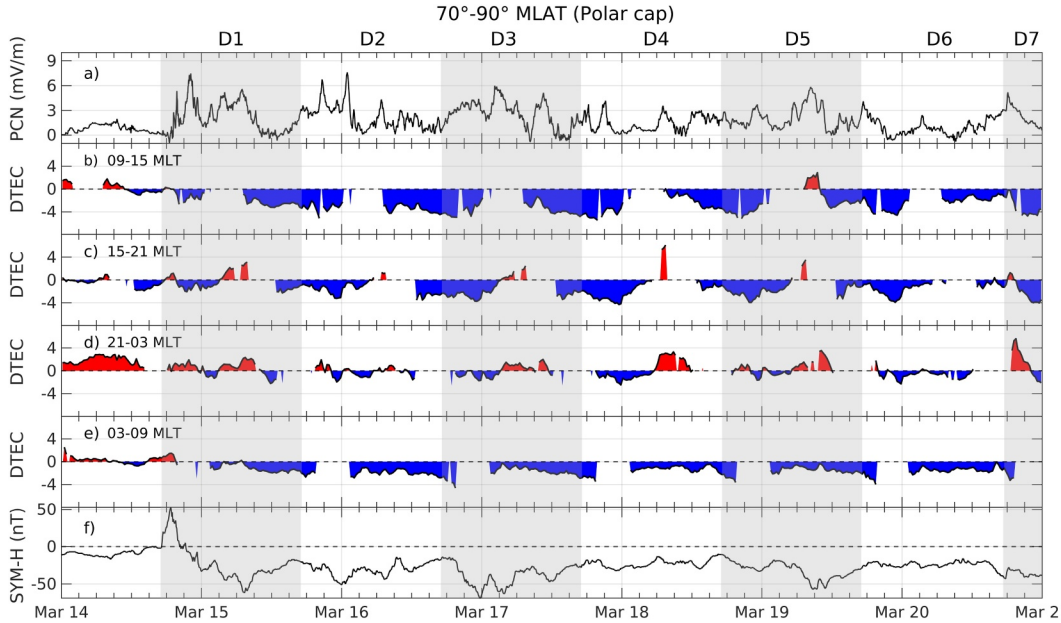

Figure 4. Parameters for 70°– 90° MLAT (polar cap). Panels from top to bottom: (a) PCN index. (b)–(e) DTEC (in unit of TECU) in the dayside (09–15 magnetic local time (MLT)), dusk sector (15–21 MLT), night sector (21-03 MLT) and dawn sector (03–09 MLT) (f) SYM-H index. The date numbers refer to 00 UT. The sequence of shaded and non-shaded periods indicate the days after the storm onset numbered D1–D7.

Figure 4 shows the mean DTEC over four MLT sectors for the polar cap. The polar cap north (PCN) index (Troshichev et al., 1988) is shown in Figure 4a, which is a proxy for the CPCP based on magnetometer measurements within the Northern polar cap (Troshichev et al., 1996).

The bottom panel shows the SYM-H index variations. Maximum values of the PCN are seen on D1 and D2 reaching approximately 8 mV/m, but also on D3 and D5 PCN reaches 6 mV/m, while D4 and D6 show smaller values. Figure 4 panels b–e show the DTEC averaged over the four MLT sectors described above, and red color

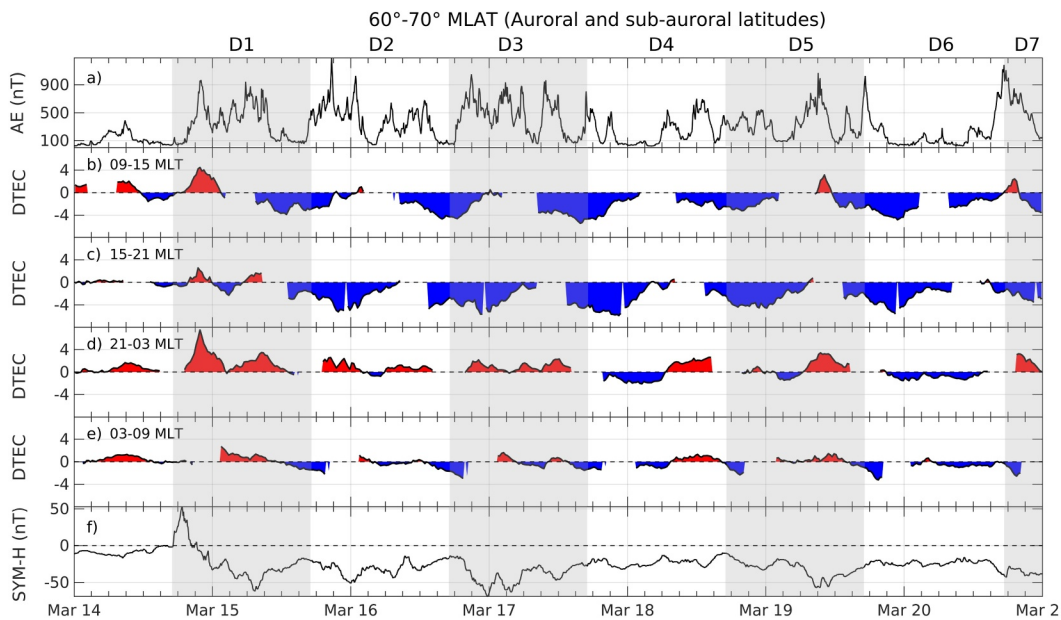

Figure 5. Same as Figure 4, but for the latitude range 60°- 70° MLAT (auroral and sub-auroral latitudes) and the top panel is changed to the AE index.

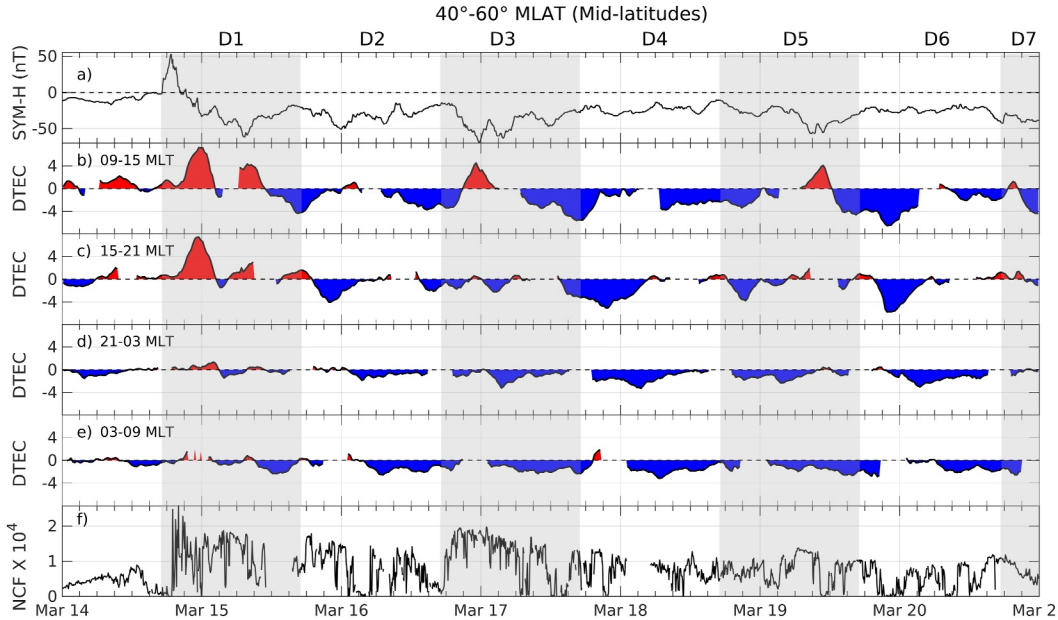

Figure 6. Same as Figure 4, but for the latitude range 40°– 60° MLAT (mid-latitudes). Also panel (a) is changed to the SYM-H index and panel (f) to the Newell coupling function.

indicates an enhancement in DTEC and blue color indicates a depletion. The gaps in DTEC curves correspond to the Siberian sector, where the number of GPS receiving stations is small. As the Earth rotates, a specific MLT time sector contains a different geographic distribution and different number of stations. Therefore, for example, within the 09–15 MLT (day) sector, right after the Siberian data gap, the MLT distribution has a bias toward 09–11 MLT and Scandinavian sector. Just before the data gap, there is a bias toward 15 MLT and the Asian sector. Therefore, this bias needs to be considered when interpreting in the diurnal variations at the different MLT sectors.

From Figure 4b, it is very evident that over the entire course of the storm until D7, TEC over the polar cap in the daytime (09–15 MLT) has decreased significantly from the quiet time level. The depletion starts to deepen with the SSC onset reaching values < -4 TECU on D2–D5 during the main phase of the storm. These values correspond to decreases of 25%–50% from the quiet time (see the supplementary Figure S1 in Supporting Information S1, where the DTEC is shown in percentage). A short-duration increase in DTEC is observed on D5 (19 March), and that is related to a polar cap patch. The same patch can be observed in the dusk (panel c) and midnight (panel d) sectors (see also the Movie S6).

Figure 4c shows the DTEC in the dusk sector (15–21 MLT), where a small enhancement in DTEC appeared in the beginning of the storm on 14 March at 19:50 UT followed by depletion. The small enhancement is associated with intense duskside Region 1 upward FAC and electron precipitation near 70° MLAT, possibly associated with auroral oval expansion to latitudes higher than 70° MLAT, but deep in the polar cap there is depletion (see the Movie S1). The dusk sector shows mostly depletions in DTEC on all days reaching < -4 TECU and 30%–50% decrease (see Figure S1 in Supporting Information S1) in TEC compared to the quiet time. In addition, short-duration DTEC enhancements are observed almost daily, which have a peak DTEC value of 6 TECU or 200% (see Figure S1 in Supporting Information S1) on 18 March and they correspond to polar cap patches.

The enhancements in Figure 4c corresponding to polar cap patches seem to have an apparent periodic structure repeating almost every day at about 06–08 UT. However, we remind the reader that Figure 4 contains data averaged over 20° MLAT and 06 MLT. In the polar cap, the main effect on the dayside and afternoon is depletion of TEC. However, patches produce enhancements in TEC. To produce an overall enhancement in this figure, the enhancement needs to cover a large area and/or be very strong compared to depletion. As patches move from the dayside toward the nightside, they tend to spread out, covering larger regions. At about 06–08 UT, the 15–18 MLT sector corresponds to the Siberian sector with very sparse data, whereas 18–21 MLT occurs within

Western North America with good coverage of data, capturing patches that have spread out. One such occasion of patch on 18 March will be discussed as an example in Section 4.2 and it is shown in Figure 9.

Figure 4d shows that in the midnight sector (21–03 MLT), increases in DTEC were more dominant than the small decreases. The enhancement before SSC is due to the substorm activity (see 2d) well before the storm. After the onset of the storm, a rise in AE index is observed and is reflected as an increase in TEC. During the substorm expansion phase, the auroral oval expands to higher latitudes, even higher than 70° MLAT. Compared to 4c, it is clear that some of the enhancements in TEC occurred at the same time as the enhancements due to polar cap patches in the dusk sector. The anti-sunward motion of the polar cap patches reaching the nightside is a major reason for these TEC enhancements in the night sector. Up to 200% (see Figure S1 in Supporting Information S1) increase in TEC is observed in the midnight sector on 18 March during an anti-sunward motion of the polar cap patch that was observed in the dusk sector.

DTEC in the dawn sector at (03–09 MLT) in Figure 4e shows again mainly depletions, except during the SSC. The depletions in TECU units are smaller in the dawn sector than in the dusk sector, but in relative units may reach 50% (see Figure S1 in Supporting Information S1).

3.3. Auroral and Sub-Auroral TEC Variations

Figure 5 shows the MLT variations of DTEC in the latitude range 60°–70° MLAT, which on the night side corresponds roughly to the auroral oval, but in the dawn to dusk sector may have a contribution from the sub-auroral region. In the day sector, under northward IMF conditions when the auroral oval is contracted, these latitudes correspond mainly to sub-auroral regions. Therefore, we have inspected the supplementary movies containing additional information of the extent of the associated convection pattern and FACs to make the more detailed interpretations discussed below.

Figure 5a shows the AE index variations during the storm. With the storm onset at 17:25 UT on 14 March, a gradual rise in the AE index can be observed. The AE index remained at high values, above 500 nT, on most of the days, indicating strong substorm activity during the geomagnetic storm. Our event also has some characteristics of the high-intensity, long-duration continuous AE activity (HILDCAAs), which are believed to be caused by large non-linear amplitude Alfvén waves in the HSSs (Tsurutani et al., 2020, & references therein).

Figure 5b shows the DTEC in the day sector (09–15 MLT). Initially an enhancement in TEC is observed on 14 March at 19–24 UT. As can be seen from Figure 3b, in the beginning of the storm main phase, increase in TEC takes place from mid-latitudes to latitudes up to 70° at midday, so the increase is a part of the storm positive phase. Increase in DTEC at 23–24 UT can be attributed to the penetration of the SED plume from the dusk-side mid-latitude to the high latitude in the post noon sector (see also Figure 3c).

After the onset of the main phase, mostly a deep depletion in DTEC is observed on the day side until D5. On D3, DTEC reached a minimum of −4 TECU, corresponding to 50% reduction (see Figure S2 in Supporting Information S1). On 19 March (D5), a positive enhancement is seen at 09–12 UT. Again, this is associated with a positive phase of the storm extending to mid-latitudes, see also Figure 3h.

Figure 5c shows that an enhancement in DTEC is also observed in the dusk (15–21 MLT) sector in the beginning of the storm on 14 March simultaneously with the dayside. A second enhancement takes place on 15 March (D1), and it is associated with the effects of polar cap patches and auroral precipitation (see the supplementary material Movie S2). DTEC showed a deep depletion on D2 to D6, reaching 50% decrease on D4 (see Figure S2 in Supporting Information S1). The depletions were somewhat larger in the dusk (panel c) than dayside (panel b) sector.

The DTEC variations in the night sector 21–03 MLT (Figure 5d) mostly show enhancements with a maximum of 6 TECU corresponding to 200% increase in TEC on 14 March (Figure S2 in Supporting Information S1) and are well correlated with the AE index (Figure 5a). At least 50% increase in TEC is observed on all days during the storm. This implies that the nightside DTEC enhancements are caused by strong auroral precipitation. Figures 3b, 3c, and 3h show examples how the auroral oval in the midnight and morning sectors is seen in global DTEC. Because of the strong auroral activity, DTEC enhancements (more than 50%, see panel d in Figure S2 in Supporting Information S1) are also observed in the dawn 03–09 MLT sector (Figure 5e). Only on the more quiet days, namely on D4 and D6, a longer duration decrease in DTEC can be seen in the midnight sector. The midnight

and dawn sectors DTEC increases and decreases mostly occur at the same times (see also Figure S2 in Supporting Information S1), indicating a common source of origin.

3.4. Mid-Latitude TEC Variations

Figure 6 shows the DTEC variations at different MLT sectors at 40° −60° MLAT corresponding roughly to mid-latitudes. During the SSC in the beginning of D1, there is a small enhancement in DTEC in the day (09–15 MLT) and dusk (15–21 MLT) sectors. With the onset of the storm main phase on 14 March at 21:15 UT (Figure 6a), the TEC increase reached 6 TECU corresponding to 50% (see Figure S3 in Supporting Information S1) increase of the quiet time level near midnight in the day (09–15 MLT) and dusk (15–21 MLT) sectors, see Figures 6b and 6c and supplementary Figure S3 in Supporting Information S1. This period of positive DTEC can be identified as a positive ionospheric storm phase and it lasted until 03 UT on 15 March. The Newell coupling function reached the highest values this time (see panel f). The positive phase is also visible in the night (21–03 MLT) and dawn (03–09 MLT) sectors, even though the increase in DTEC is smaller there.

The DTEC increase was followed by a short-duration depletion and again an enhancement, giving it a double-humped structure on D1 (Figures 6b and 6c). The second peak in DTEC at about 8 UT on D1 occurs close to the first minimum < -50 nT in the SYM-H index.

Looking at the day sector (Figure 6b), we can see additional signatures of positive storm phases on D2, D3 and D5, and all of them are associated with minima ≤ -50 nT in the SYM-H index and a high Newell coupling function. However, after D1, the day sector is dominated by negative storm phases. The depletions on the dayside reach about 30% (see Figure S3 in Supporting Information S1) compared to the background TEC.

The dusk sector (Figure 6c) shows a third maximum in DTEC in the end of D1. After D1, depletions dominate and they reach 40% compared to the background TEC, in the beginning of D4 (Figure S3 in Supporting Information S1).

Night (Figure 6d) and morning (Figure 6e) sectors also show a double positive peak in DTEC on D1, similar to what is observed in the day and dusk sectors. However, this similarity is more evident for relative changes in TEC shown in Figure S3 in Supporting Information S1 than for absolute values shown in Figure 6, since the percentage changes are as large in the night and morning sectors as on the day and dusk sectors. On the later days of the storm, mainly a depletion in TEC is observed in the night and morning sectors. The largest relative depletion in TEC takes place in the end of 17 March/beginning of 18 March in the beginning of D4 with 50% (see Figure S3 in Supporting Information S1) decrease in TEC in the night (21–03 MLT) sector. On D6 almost a similar decrease is seen. Both on D4 and D6 the SYM-H index has recovered above −16 nT and the Newell coupling function has only moderate values.

4. Discussion

4.1. Depletions in TEC

From Figures 4–6, it is clear that during the main and recovery phases of the geomagnetic storm, TEC depletions dominate in most MLT sectors at high and mid-latitudes, with the following exceptions: the midnight 21–03 MLT and morning 03–09 MLT sectors for auroral and sub-auroral latitudes, the midnight sector for polar cap, and the positive phase at mid-latitudes covering the day and dusk sectors 09–21 MLT in the beginning of the main phase on D1 (and two short-duration positive phases on D3 and D5). Each day after the storm onset until D6, TEC was decreased at least by 25% and up to 50% as compared to the background conditions in the day, dusk and dawn sectors of the polar cap, in the day and dusk sectors at auroral to sub-auroral latitudes, and in all MLT sectors at mid-latitudes after D1. Possible mechanisms that can cause the negative ionospheric storm phase are discussed below.

4.1.1. Role of Ion-Frictional Heating

Several studies have been previously conducted to understand the reason for the negative ionospheric storm phase. Many of these studies supported the notion of dynamical effects due to electric fields and neutral composition changes as the plausible mechanisms that cause the negative ionospheric storm (Prölss, 1976; Zhang et al., 2004). An increase in the ion–neutral frictional heating due to intensified electric fields at high latitude plays

a crucial role in the electron density variations during geomagnetic storms. Two important consequences of ion–neutral frictional heating are: increases in ion temperature (T_i) as well as neutral composition changes in the F region due to transport of molecular-rich air from lower altitudes owing to elevated neutral temperature (T_n). The F–region composition changes will be discussed in more detail in the next Section 4.1.2.

An increase in the ion temperature affects the reaction rates to speed up the recombination rate of O^+ ions and thereby decrease the electron density (Grandin et al., 2015; Vasyliūnas & Song, 2005; Winser et al., 1986). Sojka et al. (2009) reported a one to one correlation between CIR events and ionospheric heating in the northern polar and auroral regions using radar measurements. No global measurements of T_i are available, but a local measurement by the European Incoherent Scatter Scientific Association (EISCAT) radars during the storm shows that at high latitudes, roughly 50% of F–region electron density decreases were associated with T_i enhancements larger than 200 K (Ellahouny et al., 2024). In most cases at high latitudes, we can expect to have the combined effect of T_i increases and composition changes. Furthermore, neutral winds can carry the composition changes to regions void of frictional heating.

As Figure 2d shows, the CPCP estimate from SuperDARN exceeds 65 kV on most of the days, reaching a maximum value of 90 kV on 16 March at 00:30 UT (D2), but having high values until D6. This indicates that due to enhanced global convection electric field, we can expect the ion-frictional heating to play a major role for the TEC depletions on the day and dusk sectors in the polar cap and at auroral latitudes as seen in Figures 4 and 5.

Sub-auroral polarization streams (SAPS, Foster & Burke, 2002), which in the dusk sector are associated with strong westward plasma drifts (> 500 m/s), are often linked with electron density depletions in the dusk sector (Aa, Erickson, et al., 2020; Pintér et al., 2006; Wang et al., 2012).

To study the role of SAPS in TEC depletion in the dusk sector, we searched for DMSP conjunctions with observed TEC depletions in the dusk sector. Figure 7 shows two examples of SAPS and a simultaneous TEC depletion at the location. SAPS is usually associated with a midlatitude trough (Aa, Erickson, et al., 2020), which is a prominent plasma depletion in the F region, and lies typically between the footprints of the plasmapause and the equatorward boundary of the auroral oval, spanning a few degrees in MLAT and several hours in MLT (Aa, Zou, et al., 2020; Rodger et al., 1992). In each panel, the left plot shows the auroral emission in Lyman-Birge-Hopfield Short (LBHS) from DMSP/SSUSI measurements and overlaid on it is the cross track ion velocity. On the right side, the cross track ion velocity is overlaid on the DTEC map. In Figure 7a, the cross track ion velocity near 18 MLT equatorward of the auroral oval reaches 1,000 m/s, indicating a SAPS. In the DTEC map, TEC depletion is seen to extend 60°–70° MLAT and the equatorward edge of the depletion region (60°–62° MLAT) is observed to coexist with the SAPS. In Figure 7b near 19 MLT, the cross track ion velocity reaches more than 2,000 m/s at 57°–61° MLAT and is well outside the auroral oval as inferred from the SSUSI auroral emission. This time, a wide depletion region in TEC extends from 57° to 80° MLAT in the dusk sector. Here as well, the SAPS coexist with the equatorward part of the depletion. Hence, depletions in TEC coexist with SAPS in the dusk sector can give a contribution to our auroral and sub-auroral latitude category (event in Figures 7a and 7b) and to mid-latitude category (event in Figure 7b).

4.1.2. Neutral Composition Changes

A widely discussed mechanism for negative ionospheric storm is the neutral composition change due to increased energy input in the high latitude ionosphere–thermosphere system during geomagnetic storms (Fuller-Rowell et al., 1994; Prölss, 1997; Zhang et al., 2004). It is reported that atmospheric expansion under Joule heating can affect the mass density at F-region (Deng et al., 2009; Richmond & Lu, 2000). Higher concentrations of N_2 and O_2 accelerate the recombination reactions in the F-region resulting in the depletion of electron density. Thus it is important to study the thermospheric variations as well to understand their relative role in depleting F-region plasma.

To examine the role of neutral composition changes in the electron density depletions during this event, we compare the TEC variations with the $\sum O/N_2$ ratio derived from the TIMED/GUVI dayglow measurements. GUVI provides us with composition data near 8 MLT, which falls in the late morning MLT range.

Figure 8 shows the comparison of DTEC with GUVI $\sum O/N_2$ ratio for 14–20 March. The $\sum O/N_2$ estimates come from the sunlit part of the orbit (Christensen et al., 2003), which has an orbital period of 97 min. In Figure 8 the LST of the measurement, taken from the longitude where the TIMED satellite measurement crosses the 50°

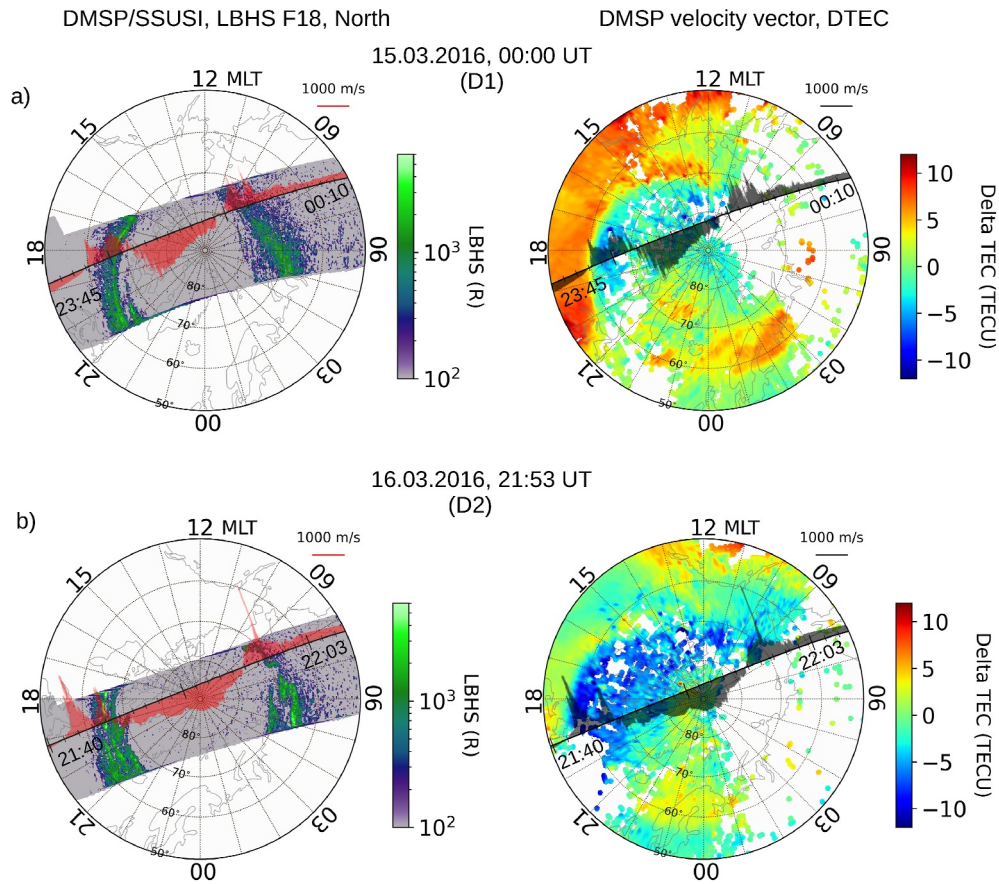

Figure 7. Instances showing SAPS and associated TEC depletion, both presented in AACGM MLT-MLAT coordinate system. On both panels, left polar plot shows the cross track ion velocity measured by DMSP F18 satellite overlaid on SSUSI LBHS emission measurements and the right plot shows the same cross track ion velocity overlaid on DTEC maps. The start and end UT times of the DMSP orbit are labeled inside.

geographic latitude, is given and it varies from 08:30 to 07:20 LST during the period of 14–20 March 2016. In each panel, the left polar plot shows the GUVI $\sum O/N_2$ gridded data product measured during 24 hr, and the corresponding UT times are given on the rim of the polar plot, where the UT time runs clockwise. Note that during 24 hr, the Earth makes one rotation, and hence each UT time corresponds to a certain geographic longitude. The discontinuity observed in the GUVI panels indicates the start/end of the day's measurement. In order to compare the TEC variations and the neutral composition changes, the polar plots of DTEC shown on the right-hand panels of Figure 8 are created in a similar manner to cover 24 hr. For DTEC plots, 24° wide longitude sectors are created, each one centered at one of the longitudes and UT times of the 15 daily GUVI overpasses. Both DTEC and $\sum O/N_2$ are plotted in the geographical polar coordinate system with a latitudinal range 30°–90°, but GUVI data is available only below about 62° geographic latitude.

Figure 8a shows the DTEC and $\sum O/N_2$ on 14 March. In this plot, 00–18 UT corresponds to the time before the storm onset, and hence we can consider the $\sum O/N_2$ values there as the background situation before the storm showing that $\sum O/N_2$ has smaller values in the latitude range 62°–50° than at lower latitudes. After the storm onset, at 21 to 24 UT, the region of small $\sum O/N_2$ covers narrower high-latitude region than before 21 UT and an enhancement in $\sum O/N_2$ is observed at mid-latitudes below 60°. In the DTEC plot, an enhancement is observed in the same 21–24 UT sector (over Japan) corresponding to the storm positive phase.

On 15 March in Figure 8b, the $\sum O/N_2$ ratio shows a significant decrease in the American sector (12–15 UT) compared to the previous day, which extends to 30° latitude. Correspondingly, a depletion in DTEC is observed in the same sector with a sharp boundary on the west coast of America, similar to the boundary of low $\sum O/N_2$ ratio.

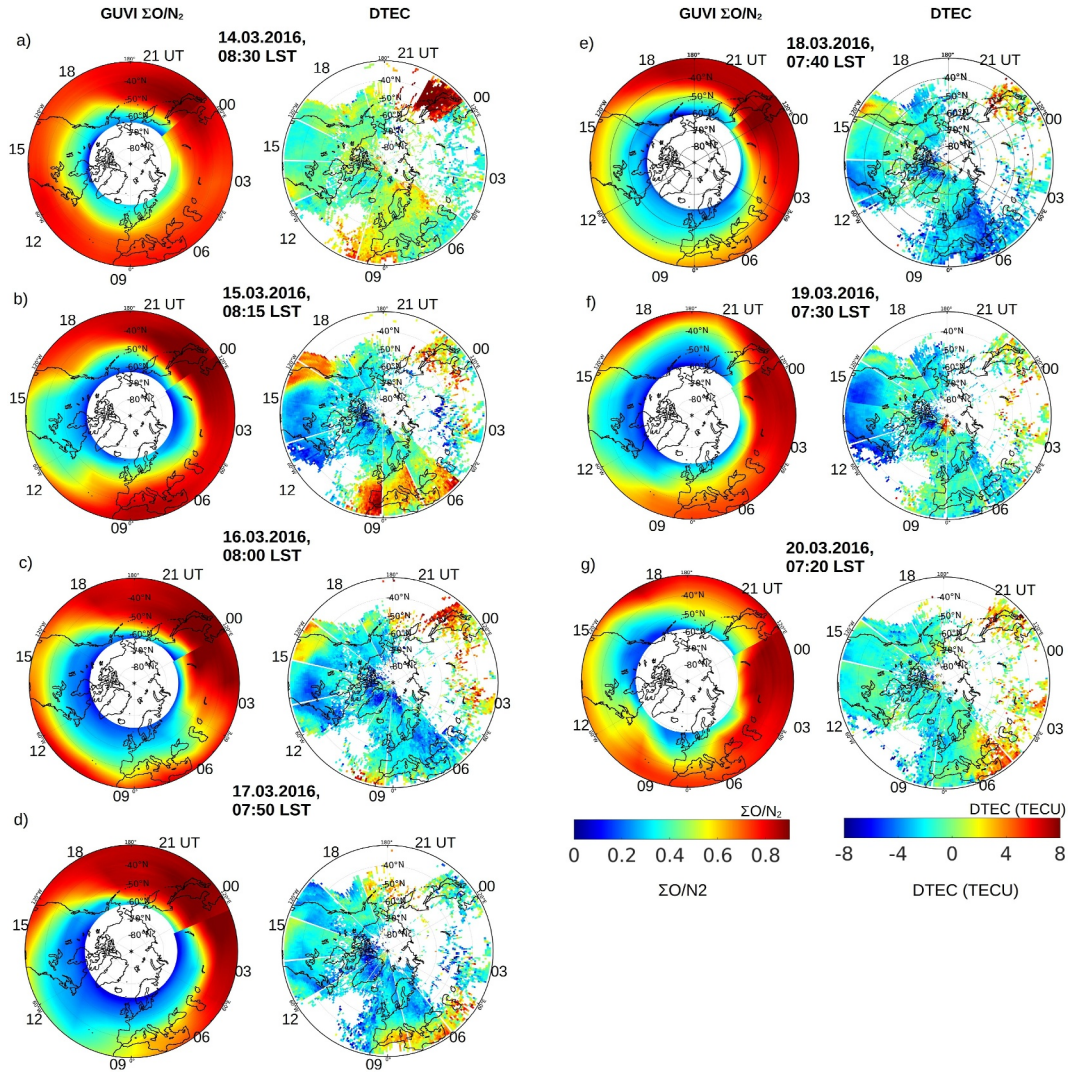

Figure 8. Panels (a)–(g) show on the left a 24-hr observation of $\sum O/N_2$ from TIMED/GUVI measured at a fixed local solar time and corresponding UT times are labeled outside, and on the right DTEC obtained by stacking sectors corresponding to GUVI observations, both plotted in geographical coordinates with a latitude range of 30° – 90°.

The $\sum O/N_2$ ratio has decreased also at other UT times at latitudes poleward of 50°, but the DTEC data is sparse there.

On 16 March in Figure 8c, the $\sum O/N_2$ disturbance covers a wider UT (and geographic longitude) region and values have become lower in the American sector than on 15 March, though the decrease does not extend as low latitudes as on the previous day. TEC depletion is observed in the corresponding region.

On 17 March in Figure 8d, the $\sum O/N_2$ values reach their minimum values and the region of low values extends to latitude of 30° on the east coast of America and west coast of Europe, with a depletion in TEC in the same region. On 18 March (Figure 8e), the composition disturbance is somewhat weaker than on the previous day, but on 19 March (Figure 8f) the composition disturbance gets again stronger, with TEC depletion also being stronger in the American sector than on the previous day. On 20 March (Figure 8g) both the composition disturbance and TEC depletion start to weaken.

In addition to the decreases in $\sum O/N_2$, increases in $\sum O/N_2$ are observed on several days. On March 14, as mentioned above, this increase, along with a rise in TEC, was seen during the positive phase of the storm at 21–24

UT at mid-latitudes near Japan. On March 15 (Figure 8b), the increase in $\sum O/N_2$ and increase in DTEC are observed in the European sector. On each day after that, several hours long increase in $\sum O/N_2$ takes place in the Asian and Siberian sectors, but those regions are very poorly covered by TEC observations, clear enhancements can be seen only occasionally near Japan. The increase in $\sum O/N_2$, as observed in various other studies as well (e.g., Lee et al., 2013; Mannucci et al., 2009; Mendillo, 2006), is mainly caused by downward vertical neutral winds and could contribute to the increase in TEC by lowering the recombination rate in the F region due to decreased N_2 and increasing the production rate due to more O in the sunlit ionosphere (Burns et al., 1995; Fuller-Rowell et al., 1994; Pedatella et al., 2010).

In summary, the data shows that in the late morning sector, a decrease of $\sum O/N_2$ and depletion in TEC occur within the same regions during the storm main phase, verifying that the composition change plays an important role in TEC depletions at geographic latitudes below 62°. Although there is some spatial correlation between the increase in $\sum O/N_2$ and the enhancements in DTEC, we cannot draw a strong conclusion about the dependence of TEC enhancements on $\sum O/N_2$ increases. This is due to the scarcity of data points in the DTEC maps in those sectors.

4.2. Enhancements in TEC

Several sources for TEC enhancements exist and they are different for different latitudes and MLT regions. In this section, we will discuss the polar cap patches, the auroral precipitation and the SED plume. The least understood phenomenon during geomagnetic storms is the positive phase (e.g., Prölss, 2006), for which a very brief summary is given here. We are carrying out a separate study of the positive phase of this storm with additional data.

In the polar cap, significant enhancements in TEC can be caused by polar cap patches. Typically, a polar cap patch is identified as an isolated structure with at least double the plasma density relative to the ambient plasma in the F-region with 100–1,000 km size (Carlson, 2012; Weber et al., 1984; Zou, Perry, & Foster, 2021). During the storm event, patches are observed mainly in the dusk sector (15–21 MLT) on days D1, D3, D4, and D5 around 03–08 UT and on D7 between 18 and 20 UT, see Figure 4c and S1.

Figure 9 shows an example of the development and transport of one polar cap patch. To clearly demonstrate that the identified structures are patches, which have clear TEC enhancements from the surrounding plasma, the absolute TEC maps (left panels) are shown alongside the DTEC maps (right panels). On 18 March, a patch becomes visible around 05:10 UT, as seen in both TEC and DTEC maps in Figure 9a on the dayside in the center of the polar cap. During that time the IMF B_z is negative, which is a favorable condition for the formation of the polar cap patch (Carlson, 2012; Jin et al., 2019). Both the IMF B_z and B_y components remain negative during the transport of the patch from the dayside to the night side. The patch is observed to move antisunward following the convection streamlines, as seen in Figure 9b (and in Movie S5). Figure 9c shows that the patch has started to move back to the dayside on the dusk convection cell following convection streamlines. The enhancement seen in the dusk sector has also some contribution from particle precipitation associated with the poleward movement of the upward FAC (see Movie S5). As B_z continues to be negative, a new patch is seen to be injected into the polar cap and to trail behind the previous patch in Figure 9d. In Figures 4c and 4d, the effect of this patch on TEC is seen both on the dusk and night MLT sectors on D4, corresponding to an increase of 3 TECU and 200% (Figure S1 in Supporting Information S1). Polar cap patches are also observed on days D1, D3, D5, and D7.

In the night sector of the polar cap, increases in TEC are more dominant than decreases. Two factors contribute to that, the polar cap patches discussed above and auroral precipitation. On 14 March, in the beginning of the storm, an increase in TEC associated with the poleward expansion of the auroral precipitation is seen between 18 and 24 UT in the polar cap night sector (see Figure 4d and Movie S1). Increases in TEC due to the poleward expansion of the auroral oval are seen on days D4 and D7 as well.

Within the auroral oval, we expect to see the effects of particle precipitation (Tesfaw et al., 2023, & references therein). Figure 10a shows the relative variations in TEC compared to the background quiet TEC in night side auroral oval. A significant enhancement in TEC, exceeding 50%, is observed on all days. On day D1, more than 200% increase in TEC is noted. Figure 10b shows the AE index, which shows a series of substorms during the storm. To compare with the DTEC variations, AE index is only plotted for periods with enough DTEC data points. It is clearly observed that the temporal behavior of the AE index is very similar to that of the relative TEC variations in the night side auroral oval. During substorms, particle precipitation can increase the electron density

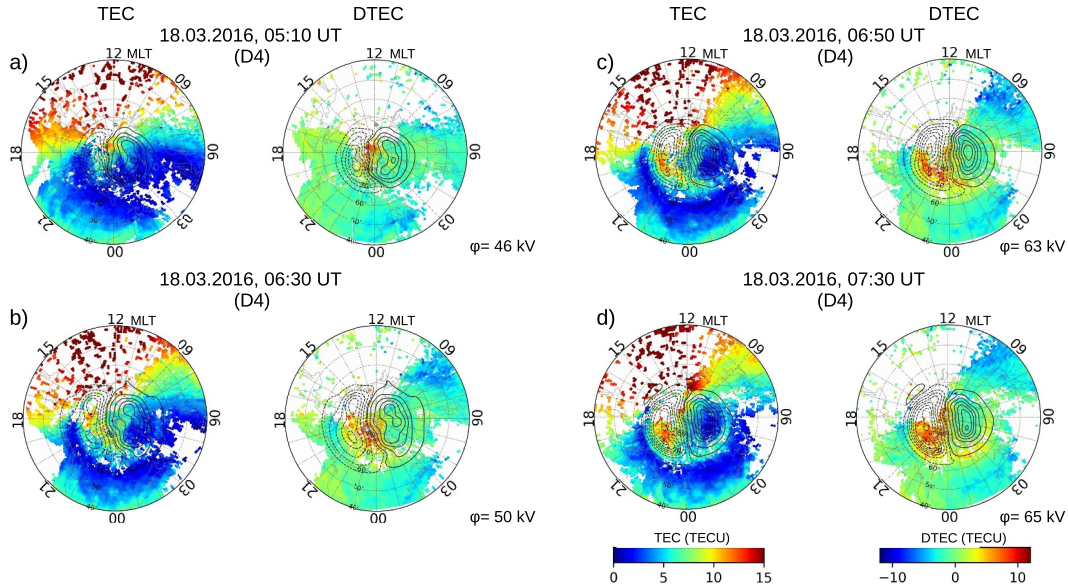

Figure 9. An example of the development of polar cap patch on March 18 (D4) of the storm. TEC on the left panels and DTEC on right panels, both presented in AACGM MLT-MLAT coordinate system. (a) Patch is located in the center of the polar cap. (b) Patch has extended to the night side. (c) Patch has become elongated to the duskside convection stream lines. (d) Patch has further spread and possibly a new patch has appeared to the center of the polar cap.

in the E–region (Aikio et al., 2002; Partamies et al., 2011; Tesfaw et al., 2022). As TEC is the column-integrated electron density, this enhancement in the E–region will be reflected in TEC values as well. Ren et al. (2020) simulated with TIEGCM an increase of TEC by 2 TECU in the nightside auroral oval owing to particle precipitation during the recovery phase of an HSS driven storm. In our case, we observe regionally averaged increases up to 6 TECU (Figure 5) during the storm.

An interesting feature in Figure 10 is that during the AE minima on D2, D4 and D6, indicating less activity and auroral precipitation, TEC values are decreased below the background (blue color). In the auroral oval, two competing processes may be operating: ion-neutral frictional heating causing TEC decreases and auroral

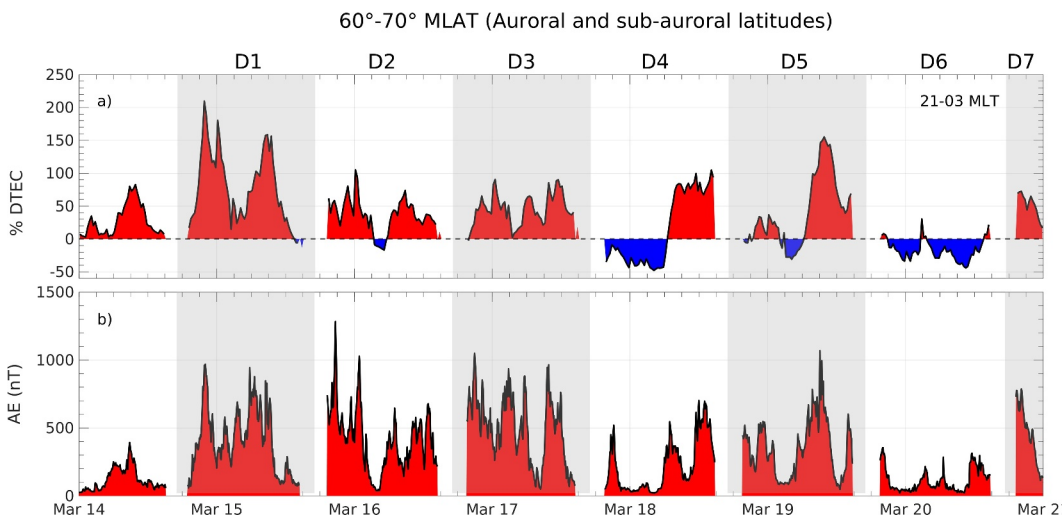

Figure 10. DTEC enhancements at 60°–70° (auroral and sub-auroral latitudes in the night sector (21-03 MLT)). (a) DTEC in percentage, (b) AE index. For comparison, AE index is plotted only when there are sufficient data points in DTEC.

precipitation causing TEC increases. The dawn sector (Figure 5) shows predominantly simultaneous TEC increases with the night sector, but the dusk sector shows mainly decreases, suggesting that ion neutral frictional heating in the dusk sector dominates over auroral precipitation.

In the beginning of the storm on D1 at auroral and sub-auroral latitudes on the dayside, 4 TECU and 30% increase (Figure 5 and Figure S2 in Supporting Information S1) in TEC at 19–24 UT are observed, produced by the SED in the post-noon sector during the storm positive phase (Foster et al., 2005). Later a SED plume (Figure 3c) developed, which is formed by the transport of F–region plasma from mid latitudes in the dusk sector toward the magnetic noon by convection streamlines (Foster, 1993; Foster et al., 2021). Zou, Ren, et al. (2021) also reported the formation of SED plume during the positive phase of a CIR–generated storm.

A positive ionospheric storm observed at the mid-latitudes in the day and dusk sectors on D1 commenced around 19 UT, after the SSC peak and intensified with the onset of the main phase. This enhancement in TEC continued for 9 hr until 03 UT on 15 March. Various studies have addressed the dayside positive ionospheric storm phase during geomagnetic storms. Some potential mechanisms that can cause the positive ionospheric storms are: uplifting of the plasma to altitudes of lower recombination rate by the southward neutral winds or eastward electric fields, traveling ionospheric or atmospheric disturbances, and increase in oxygen density due to atmospheric downwelling (Buonsanto, 1999; Mendillo, 2006; Prölss, 1995, 2006, 2008). A more detailed analysis has to be done to understand the dominant mechanism that causes the dayside positive ionospheric storm phase and is out of the scope of this paper.

5. Conclusions

The moderate (SYM-H minimum −65 nT) and long-lasting HSS/SIR-driven storm near spring equinox 14–20 March 2016 was studied by using GNSS TEC data and complementary measurements from other instruments including $\sum O/N_2$ from TIMED GUVI and DMSP ion drift. The storm commenced with SSC on 14 March 2016 at 17:20 UT, which is taken as the start of the first storm day D1. The storm lasted for almost seven days with four SYM-H minima less than −50 nT. The background TEC, calculated by taking the mean of four quietest days of the month, was removed from the observed TEC, yielding the storm-induced changes in TEC. Below, we summarize separately the results for TEC depletions and increases.

5.1. TEC Depletions

- The storm caused daily 25%–50% depletions in TEC for six days in the day, dusk and dawn MLT sectors of the polar cap, in the day and dusk sectors at auroral and sub-auroral latitudes, and after D1 in all MLT sectors at mid-latitudes. As discussed in several earlier papers, depletions most likely are associated with ion-neutral frictional heating causing ion temperature enhancements and neutral composition changes in the F region, both increasing recombination of O^+ ions.
- TIMED/GUVI measurements in the late morning at about 8 LST showed $\sum O/N_2$ decreases at mid-latitudes that spatially correlated with TEC depletions, further supporting the suggestion that composition change is important for the mid-latitude negative phase.
- At sub-auroral latitudes, SAPS produced localized TEC depletions. In this study, they were identified predominantly from the dusk sector and in the examples studied covered a narrow latitude region of a few degrees.

5.2. TEC Enhancements

- In the initial phase and in the beginning of the main phase on D1, a strong (50%) and long–lasting (9 hr) increase in TEC (the positive phase of the storm) was observed at mid-latitudes. It had a peak amplitude in the day and dusk sectors and smaller amplitudes in the night and dawn sectors.
- In the day and dusk sectors an increase in TEC was observed at 60°–70° MLAT in the beginning of the main phase on D1 for about 6 hr, simultaneously with the mid-latitude positive phase. The SED plume developed in the post-noon sector as the convection pattern suddenly expanded and captured some mid-latitude plasma to higher latitudes.
- In the polar cap, the polar cap patches originating from the dayside and moving with plasma convection toward the night increased TEC up to 200%.

- In the nightside and morning sectors of auroral latitudes, the dominant feature throughout the storm was TEC increase, which was produced by auroral precipitation, as indicated by the strong correlation with the AE index and spatial distribution within the auroral oval. The maximum values occurred in the beginning of the storm main phase with locally averaged values reaching 6 TECU and 200%.

Data Availability Statement

The GNSS TEC data used in this study is obtained from the Madrigal database at http://cedar.openmadrigal.org. The TEC maps were projected in AACGM coordinate system using GeospaceLab (https://github.com/JouleCai/geospacelab). Field Alligned Currents data and electric potential were obtained from https://ampere.jhuapl.edu/info/ and http://vt.superdarn.org/plot/convection-maps. $\sum O/N_2$ data can be accessed at http://guvitimed.jhuapl.edu/data_use and cross–track ion velocity and auroral emission data is obtained from https://www.ngdc.noaa.gov/stp/satellite/dmsp/. Data for the solar wind, IMF and geomagnetic indices were taken from the OMNI data base at (https://omniweb.gsfc.nasa.gov/form/omni_min.html).

Acknowledgments
This work was supported by the International Space Science Institute (ISSI) in Bern through ISSI International Team project #487, and by Kvantum Institute project Arctic Ionospheric Response to Space Weather Events, and by Research Council of Finland projects 348782 and 354521. A part of the work of S.-I. Oyama was supported by JSPS KAKENHI 21KK0059, 21H04518, 22K21345, 22H00173, 23K22554, and was carried out by the joint research program of Planetary Plasma and Atmospheric Research Center, Tohoku University. A. Maute was supported by NASA award 80NSSC20K1784. The authors thank Massachusetts Institute of Technology for providing the access and use of GNSS TEC data under support from the U.S. National Science Foundation via Madrigal databaseGrant AGS-AGS-195273. We acknowledge use of NASA/GSFC's Space Physics Data Facility's CDAWeb service and OMNI data for providing magnetic indices and solar wind parameters. We thank the AMPERE team and the AMPERE Science Data Center for providing data products derived from the Iridium Communications constellation, enabled by support from the National Science Foundation. The GUVI data used here are provided through support from the NASA MO&DA program. The GUVI instrument was designed and built by The Aerospace Corporation and The Johns Hopkins University. The Principal Investigator is Dr. Larry J. Paxton. We acknowledge the use of SuperDARN data. SuperDARN is a network of radars funded by national scientific funding agencies of Australia, Canada, China, France, Italy, Japan, Norway, South Africa, the United Kingdom, and the United States of America. The authors thank Dr. Kevin Martin at Boston College for valuable discussion on the data quality of the DMSP cross-track ion velocity.

References

Aa, E., Erickson, P., Zhang, S.-R., Zou, S., Coster, A., Goncharenko, L., & Foster, J. (2020). A statistical study of the subauroral polarization stream over north American sector using the millstone hill incoherent scatter radar 1979–2019 measurements. *Journal of Geophysical Research: Space Physics*, *125*(10). https://doi.org/10.1029/2020JA028584

Aa, E., Zou, S., Erickson, P. J., Zhang, S.-R., & Liu, S. (2020). Statistical analysis of the main ionospheric trough using swarm in situ measurements. *Journal of Geophysical Research: Space Physics*, *125*(3), e2019JA027583. https://doi.org/10.1029/2019JA027583

Aikio, A. T., Lakkala, T., Kozlovsky, A., & Williams, P. J. S. (2002). Electric fields and currents of stable drifting auroral arcs in the evening sector. *Journal of Geophysical Research*, *107*(A12). SIA 3-1–SIA 3-14. https://doi.org/10.1029/2001JA009172

Anderson, B. J., Korth, H., Waters, C. L., Green, D. L., Merkin, V. G., Barnes, R. J., & Dyrud, L. P. (2014). Development of large-scale Birkeland currents determined from the Active Magnetosphere and Planetary Electrodynamics Response Experiment. *Geophysical Research Letters*, *41*(9), 3017–3025. https://doi.org/10.1002/2014GL059941

Anderson, B. J., Takahashi, K., & Toth, B. A. (2000). Sensing global birkeland currents with iridium® engineering magnetometer data. *Geophysical Research Letters*, *27*(24), 4045–4048. https://doi.org/10.1029/2000GL000094

Anderson, B. J., Waters, C., Green, D., & Stauning, P. (2008). Statistical birkeland current distributions from magnetic field observations by the iridium constellation. *Annales Geophysicae*, *26*(3), 671–687. https://doi.org/10.5194/angeo-26-671-2008

Belcher, J., & Davis, L. Jr. (1971). Large-amplitude alfvén waves in the interplanetary medium, 2. *Journal of Geophysical Research*, *76*(16), 3534–3563. https://doi.org/10.1029/JA076i016p03534

Buonsanto, M. (1999). Ionospheric storms — A review. *Space Science Reviews*, *88*(3/4), 563–601. https://doi.org/10.1023/A:1005107532631

Buresova, D., Lastovicka, J., Hejda, P., & Bochnicek, J. (2014). Ionospheric disturbances under low solar activity conditions. *Advances in Space Research*, *54*(2), 185–196. https://doi.org/10.1016/j.asr.2014.04.007

Burns, A., Killeen, T., Carignan, G., & Roble, R. (1995). Large enhancements in the O/N_2 ratio in the evening sector of the winter hemisphere during geomagnetic storms. *Journal of Geophysical Research*, *100*(A8), 14661–14671. https://doi.org/10.1029/94JA03235

Burns, A., Solomon, S., Qian, L., Wang, W., Emery, B., Wiltberger, M., & Weimer, D. (2012). The effects of corotating interaction region/high speed stream storms on the thermosphere and ionosphere during the last solar minimum. *Journal of Atmospheric and Solar-Terrestrial Physics*, *83*, 79–87. https://doi.org/10.1016/j.jastp.2012.02.006

Cai, L., Aikio, A., Kullen, A., Deng, Y., Zhang, Y., Zhang, S.-R., et al. (2022). Geospacelab: Python package for managing and visualizing data in space physics. *Frontiers in Astronomy and Space Sciences*, *9*. https://doi.org/10.3389/fspas.2022.1023163

Carlson, H. C. (2012). Sharpening our thinking about polar cap ionospheric patch morphology, research, and mitigation techniques. *Radio Science*, *47*(4). https://doi.org/10.1029/2011RS004946

Carlson, H. C. Jr., Oksavik, K., Moen, J., & Pedersen, T. (2004). Ionospheric patch formation: Direct measurements of the origin of a polar cap patch. *Geophysical Research Letters*, *31*(8). https://doi.org/10.1029/2003GL018166

Chisham, G., Lester, M., Milan, S., Freeman, M., Bristow, W., Grocott, A., et al. (2007). A decade of the super dual auroral radar network (superdarn): Scientific achievements, new techniques and future directions. *Surveys in Geophysics*, *28*(1), 33–109. https://doi.org/10.1007/s10712-007-9017-8

Christensen, A., Paxton, L., Avery, S., Craven, J., Crowley, G., Humm, D., et al. (2003). Initial observations with the global ultraviolet imager (GUVI) in the NASA timed satellite mission. *Journal of Geophysical Research*, *108*(A12). https://doi.org/10.1029/2003JA009918

Coxon, J. C., Milan, S. E., & Anderson, B. J. (2018). A review of birkeland current research using ampere. In *Electric currents in geospace and beyond* (pp. 257–278). American Geophysical Union (AGU). https://doi.org/10.1002/9781119324522.ch16

Crowley, G., Reynolds, A., Thayer, J. P., Lei, J., Paxton, L. J., Christensen, A. B., et al. (2008). Periodic modulations in thermospheric composition by solar wind high speed streams. *Geophysical Research Letters*, *35*(21). https://doi.org/10.1029/2008GL035745

Davis, T. N., & Sugiura, M. (1966). Auroral electrojet activity index ae and its universal time variations. *Journal of Geophysical Research (1896-1977)*, *71*(3), 785–801. https://doi.org/10.1029/JZ071i003p00785

Deng, Y., Maute, A., Richmond, A. D., & Roble, R. G. (2009). Impact of electric field variability on joule heating and thermospheric temperature and density. *Geophysical Research Letters*, *36*(8). https://doi.org/10.1029/2008GL036916

Denton, M. H., Borovsky, J. E., Skoug, R. M., Thomsen, M. F., Lavraud, B., Henderson, M. G., et al. (2006). Geomagnetic storms driven by icme- and cir-dominated solar wind. *Journal of Geophysical Research*, *111*(A7). https://doi.org/10.1029/2005JA011436

Denton, M. H., Ulich, T., & Turunen, E. (2009). Modification of midlatitude ionospheric parameters in the f2 layer by persistent high-speed solar wind streams. *Space Weather*, *7*(4). https://doi.org/10.1029/2008SW000443

Ellahouny, N. M., Aikio, A. T., Vanhamäki, H., Virtanen, I. I., Cai, L., Marchaudon, A., et al. (2024). Eiscat observations of depleted high-latitude f-region during an HSS/SIR-driven magnetic storm. *Journal of Geophysical Research: Space Physics*, *129*(9). https://doi.org/10.1029/2024JA032910

Foster, J. C. (1993). Storm time plasma transport at middle and high latitudes. *Journal of Geophysical Research*, *98*(A2), 1675–1689. https://doi.org/10.1029/92JA02032

Foster, J. C., & Burke, W. J. (2002). Saps: A new categorization for sub-auroral electric fields. *Eos, Transactions American Geophysical Union*, *83*(36), 393–394. https://doi.org/10.1029/2002EO000289

Foster, J. C., Coster, A. J., Erickson, P. J., Holt, J. M., Lind, F. D., Rideout, W., et al. (2005). Multiradar observations of the polar tongue of ionization. *Journal of Geophysical Research*, *110*(A9). https://doi.org/10.1029/2004JA010928

Foster, J. C., Zou, S., Heelis, R. A., & Erickson, P. J. (2021). Ionospheric storm-enhanced density plumes. In *Ionosphere dynamics and applications* (pp. 115–126). American Geophysical Union (AGU). https://doi.org/10.1002/9781119815617.ch6

Fuller-Rowell, T. J., Codrescu, M. V., Moffett, R. J., & Quegan, S. (1994). Response of the thermosphere and ionosphere to geomagnetic storms. *Journal of Geophysical Research*, *99*(A3), 3893–3914. https://doi.org/10.1029/93JA02015

Gonzalez, W. D., Joselyn, J. A., Kamide, Y., Kroehl, H. W., Rostoker, G., Tsurutani, B. T., & Vasyliunas, V. M. (1994). What is a geomagnetic storm? *Journal of Geophysical Research*, *99*(A4), 5771–5792. https://doi.org/10.1029/93JA02867

Grandin, M., Aikio, A. T., & Kozlovsky, A. (2019). Properties and geoeffectiveness of solar wind high-speed streams and stream interaction regions during solar cycles 23 and 24. *Journal of Geophysical Research: Space Physics*, *124*(6), 3871–3892. https://doi.org/10.1029/2018JA026396

Grandin, M., Aikio, A. T., Kozlovsky, A., Ulich, T., & Raita, T. (2015). Effects of solar wind high-speed streams on the high-latitude ionosphere: Superposed epoch study. *Journal of Geophysical Research: Space Physics*, *120*(12), 10669–10687. https://doi.org/10.1002/2015JA021785

Heelis, R. A., & Sojka, J. J. (2011). Response of the topside ionosphere to high-speed solar wind streams. *Journal of Geophysical Research*, *116*(A11). https://doi.org/10.1029/2011JA016739

Jin, Y., Xing, Z., Zhang, Q., Wang, Y., & Ma, Y. (2019). Polar cap patches observed by the eiscat svalbard radar: A statistical study of its dependence on the solar wind and IMF conditions. *Journal of Atmospheric and Solar-Terrestrial Physics*, *192*, 104768. (Space Science for Sustainability). https://doi.org/10.1016/j.jastp.2018.01.011

Kavanagh, A. J., Honary, F., Donovan, E. F., Ulich, T., & Denton, M. H. (2012). Key features of >30 kev electron precipitation during high speed solar wind streams: A superposed epoch analysis. *Journal of Geophysical Research*, *117*(A9). https://doi.org/10.1029/2011JA017320

King, J. H., & Papitashvili, N. E. (2005). Solar wind spatial scales in and comparisons of hourly Wind and ACE plasma and magnetic field data. *Journal of Geophysical Research (Space Physics)*, *110*(A2), A02104. https://doi.org/10.1029/2004JA010649

Krieger, A. S., Timothy, A. F., & Roelof, E. C. (1973). A coronal hole and its identification as the source of a high velocity solar wind stream. *Solar Physics*, *29*(2), 505–525. https://doi.org/10.1007/BF00150828

Lakhina, G. S., & Tsurutani, B. T. (2016). Geomagnetic storms: Historical perspective to modern view. *Geoscience Letters*, *3*, 1–11. https://doi.org/10.1186/s40562-016-0037-4

Lee, W. K., Kil, H., Paxton, L. J., Zhang, Y., & Shim, J. S. (2013). The effect of geomagnetic-storm-induced enhancements to ionospheric emissions on the interpretation of the timed/guvi O/N_2 ratio. *Journal of Geophysical Research: Space Physics*, *118*(12), 7834–7840. https://doi.org/10.1002/2013JA019132

Lei, J., Thayer, J. P., Forbes, J. M., Sutton, E. K., & Nerem, R. S. (2008). Rotating solar coronal holes and periodic modulation of the upper atmosphere. *Geophysical Research Letters*, *35*(10). https://doi.org/10.1029/2008GL033875

Lei, J., Thayer, J. P., Wang, W., & McPherron, R. L. (2011). Impact of CIR storms on thermosphere density variability during the solar minimum of 2008. *Solar Physics*, *274*(1–2), 427–437. https://doi.org/10.1007/s11207-010-9563-y

Mannucci, A. J., Tsurutani, B. T., Kelley, M. C., Iijima, B. A., & Komjathy, A. (2009). Local time dependence of the prompt ionospheric response for the 7, 9, and 10 November 2004 superstorms. *Journal of Geophysical Research*, *114*(A10). https://doi.org/10.1029/2009JA014043

Marchaudon, A., Blelly, P.-L., Grandin, M., Aikio, A., Kozlovsky, A., & Virtanen, I. (2018). Ipim modeling of the ionospheric f2 layer depletion at high latitudes during a high-speed stream event. *Journal of Geophysical Research: Space Physics*, *123*(8), 7051–7066. https://doi.org/10.1029/2018JA025744

Mendillo, M. (2006). Storms in the ionosphere: Patterns and processes for total electron content. *Reviews of Geophysics*, *44*(4). https://doi.org/10.1029/2005RG000193

Moen, J., Oksavik, K., Alfonsi, L., Daabakk, Y., Romano, V., & Spogli, L. (2013). Space weather challenges of the polar cap ionosphere. *J. Space Weather Space Clim.*, *3*, A02. https://doi.org/10.1051/swsc/2013025

Newell, P. T., Sotirelis, T., Liou, K., Meng, C.-I., & Rich, F. J. (2006). Cusp latitude and the optimal solar wind coupling function. *Journal of Geophysical Research*, *111*(A9). https://doi.org/10.1029/2006JA011731

Partamies, N., Juusola, L., Tanskanen, E., Kauristie, K., Weygand, J. M., & Ogawa, Y. (2011). Substorms during different storm phases. *Annales Geophysicae*, *29*(11), 2031–2043. https://doi.org/10.5194/angeo-29-2031-2011

Paxton, L., Morrison, D., Zhang, Y., Kil, H., Wolven, B., Ogorzalek, B., et al. (2002). Validation of remote sensing products produced by the special sensor ultraviolet scanning imager (SSUSI): A far uv-imaging spectrograph on dmsp f-16. In *Proc. SPIE*. https://doi.org/10.1117/12.454268.4485.

Pedatella, N. M., Lei, J., Thayer, J. P., & Forbes, J. M. (2010). Ionosphere response to recurrent geomagnetic activity: Local time dependency. *Journal of Geophysical Research*, *115*(A2). https://doi.org/10.1029/2009JA014712

Phillips, J. L., Bame, S. J., Feldman, W. C., Gosling, J. T., Hammond, C. M., McComas, D. J., et al. (1995). Ulysses solar wind plasma observations at high southerly latitudes. *Science*, *268*(5213), 1030–1033. https://doi.org/10.1126/science.268.5213.1030

Pintér, B., Thom, S. D., Balthazor, R., Vo, H., & Bailey, G. J. (2006). Modeling subauroral polarization streams equatorward of the plasmapause footprints. *Journal of Geophysical Research*, *111*(A10). https://doi.org/10.1029/2005JA011457

Prölss, G. (1976). On explaining the negative phase of ionospheric storms. *Planetary and Space Science*, *24*(6), 607–609. https://doi.org/10.1016/0032-0633(76)90140-9

Prölss, G. W. (1980). Magnetic storm associated perturbations of the upper atmosphere: Recent results obtained by satellite-borne gas analyzers. *Reviews of Geophysics*, *18*(1), 183–202. https://doi.org/10.1029/RG018i001p00183

Prölss, G. W. (1995). Ionospheric f-region storms. In *Handbook of atmospheric electrodynamics* (pp. 195–248). CRC press.

Prölss, G. W. (1997). Magnetic storm associated perturbations of the upper atmosphere. In *Magnetic storms* (pp. 227–241). American Geophysical Union (AGU). https://doi.org/10.1029/GM098p0227

Prölss, G. W. (2006). Ionospheric f-region storms: Unsolved problems. In *In characterising the ionosphere*.

Prölss, G. W. (2008). Ionospheric storms at mid-latitude: A short review. In *Midlatitude ionospheric dynamics and disturbances* (pp. 9–24). American Geophysical Union (AGU). https://doi.org/10.1029/181GM03

Ren, D., Lei, J., Zhou, S., Li, W., Huang, F., Luan, X., et al. (2020). High-speed solar wind imprints on the ionosphere during the recovery phase of the august 2018 geomagnetic storm. *Space Weather*, *18*(7). https://doi.org/10.1029/2020SW002480

Rich, F. J., & Hairston, M. (1994). Large-scale convection patterns observed by dmsp. *Journal of Geophysical Research*, *99*(A3), 3827–3844. https://doi.org/10.1029/93JA03296

Richardson, I. G. (2018). Solar wind stream interaction regions throughout the heliosphere. *Living Reviews in Solar Physics*, *15*(1), 1. https://doi.org/10.1007/s41116-017-0011-z

Richmond, A., & Lu, G. (2000). Upper-atmospheric effects of magnetic storms: A brief tutorial. *Journal of Atmospheric and Solar-Terrestrial Physics*, *62*(12), 1115–1127. https://doi.org/10.1016/S1364-6826(00)00094-8

Rideout, W. C., & Coster, A. J. (2006). Automated gps processing for global total electron content data. *GPS Solutions*, *10*(3), 219–228. https://doi.org/10.1007/s10291-006-0029-5

Rodger, A., Moffett, R., & Quegan, S. (1992). The role of ion drift in the formation of ionisation troughs in the mid- and high-latitude ionosphere —A review. *Journal of Atmospheric and Terrestrial Physics*, *54*(1), 1–30. https://doi.org/10.1016/0021-9169(92)90082-V

Ruohoniemi, J. M., & Baker, K. B. (1998). Large-scale imaging of high-latitude convection with super dual auroral radar network hf radar observations. *Journal of Geophysical Research*, *103*(A9), 20797–20811. https://doi.org/10.1029/98JA01288

Sheeley, N., Harvey, J., & Feldman, W. (1976). Coronal holes, solar wind streams, and recurrent geomagnetic disturbances: 1973–1976. *Solar Physics*, *49*(2), 271–278. https://doi.org/10.1007/BF00162451

Shepherd, S. G. (2014). Altitude-adjusted corrected geomagnetic coordinates: Definition and functional approximations. *Journal of Geophysical Research: Space Physics*, *119*(9), 7501–7521. https://doi.org/10.1002/2014JA020264

Smith, E. J., & Wolfe, J. H. (1976). Observations of interaction regions and corotating shocks between one and five au: Pioneers 10 and 11. *Geophysical Research Letters*, *3*(3), 137–140. https://doi.org/10.1029/GL003i003p00137

Sojka, J. J., McPherron, R. L., van Eyken, A. P., Nicolls, M. J., Heinselman, C. J., & Kelly, J. D. (2009). Observations of ionospheric heating during the passage of solar coronal hole fast streams. *Geophysical Research Letters*, *36*(19). https://doi.org/10.1029/2009GL039064

Tesfaw, H. W., Virtanen, I. I., & Aikio, A. T. (2023). Characteristics of auroral electron precipitation at geomagnetic latitude 67° over tromsø. *Journal of Geophysical Research: Space Physics*, *128*(7), e2023JA031382. https://doi.org/10.1029/2023JA031382

Tesfaw, H. W., Virtanen, I. I., Aikio, A. T., Nel, A., Kosch, M., & Ogawa, Y. (2022). Precipitating electron energy spectra and auroral power estimation by incoherent scatter radar with high temporal resolution. *Journal of Geophysical Research: Space Physics*, *127*(4), e2021JA029880. https://doi.org/10.1029/2021JA029880

Thayer, J. P., Lei, J., Forbes, J. M., Sutton, E. K., & Nerem, R. S. (2008). Thermospheric density oscillations due to periodic solar wind high-speed streams. *Journal of Geophysical Research*, *113*(A6). https://doi.org/10.1029/2008JA013190

Thomas, E. G., & Shepherd, S. G. (2018). Statistical patterns of ionospheric convection derived from mid-latitude, high-latitude, and polar superdarn hf radar observations. *Journal of Geophysical Research: Space Physics*, *123*(4), 3196–3216. https://doi.org/10.1002/2018JA025280

Troshichev, O., Andrezen, V., Vennerstrøm, S., & Friis-Christensen, E. (1988). Magnetic activity in the polar cap—A new index. *Planetary and Space Science*, *36*(11), 1095–1102. https://doi.org/10.1016/0032-0633(88)90063-3

Troshichev, O., Hayakawa, H., Matsuoka, A., Mukai, T., & Tsuruda, K. (1996). Cross polar cap diameter and voltage as a function of pc index and interplanetary quantities. *Journal of Geophysical Research*, *101*(A6), 13429–13435. https://doi.org/10.1029/95JA03672

Tsurutani, B. T., Gonzalez, W. D., Gonzalez, A. L. C., Tang, F., Arballo, J. K., & Okada, M. (1995). Interplanetary origin of geomagnetic activity in the declining phase of the solar cycle. *Journal of Geophysical Research*, *100*(A11), 21717–21733. https://doi.org/10.1029/95JA01476

Tsurutani, B. T., Lakhina, G. S., & Hajra, R. (2020). The physics of space weather/solar-terrestrial physics (STP): What we know now and what the current and future challenges are. *Nonlinear Processes in Geophysics*, *27*(1), 75–119. https://doi.org/10.5194/npg-27-75-2020

Tsurutani, B. T., McPherron, R. L., Gonzalez, W. D., Lu, G., Gopalswamy, N., & Guarnieri, F. L. (2006). Magnetic storms caused by corotating solar wind streams. In *Recurrent magnetic storms: Corotating solar wind streams* (pp. 1–17). American Geophysical Union (AGU). https://doi.org/10.1029/167GM03

Tulasi Ram, S., Lei, J., Su, S.-Y., Liu, C. H., Lin, C. H., & Chen, W. S. (2010). Dayside ionospheric response to recurrent geomagnetic activity during the extreme solar minimum of 2008. *Geophysical Research Letters*, *37*(2). https://doi.org/10.1029/2009GL041038

Vasyliūnas, V. M., & Song, P. (2005). Meaning of ionospheric joule heating. *Journal of Geophysical Research*, *110*(A2). https://doi.org/10.1029/2004JA010615

Verkhoglyadova, O. P., Tsurutani, B. T., Mannucci, A. J., Mlynczak, M. G., Hunt, L. A., & Runge, T. (2013). Variability of ionospheric tec during solar and geomagnetic minima (2008 and 2009): External high speed stream drivers. *Annales Geophysicae*, *31*(2), 263–276. https://doi.org/10.5194/angeo-31-263-2013

Vierinen, J., Coster, A. J., Rideout, W. C., Erickson, P. J., & Norberg, J. (2016). Statistical framework for estimating GNSS bias. *Atmospheric Measurement Techniques*, *9*(3), 1303–1312. https://doi.org/10.5194/amt-9-1303-2016

Wang, W., Lei, J., Burns, A. G., Qian, L., Solomon, S. C., Wiltberger, M., & Xu, J. (2011). Ionospheric day-to-day variability around the whole heliosphere interval in 2008. *Solar Physics*, *274*(1–2), 457–472. https://doi.org/10.1007/s11207-011-9747-0

Wang, W., Talaat, E. R., Burns, A. G., Emery, B., Hsieh, S.-y., Lei, J., & Xu, J. (2012). Thermosphere and ionosphere response to subauroral polarization streams (SAPS): Model simulations. *Journal of Geophysical Research*, *117*(A7). https://doi.org/10.1029/2012JA017656

Wanliss, J., & Showalter, K. (2006). High-resolution global storm index: Dst versus sym-h. *Journal of Geophysical Research*, *111*(A2). https://doi.org/10.1029/2005JA011034

Weber, E. J., Buchau, J., Moore, J. G., Sharber, J. R., Livingston, R. C., Winningham, J. D., & Reinisch, B. W. (1984). F layer ionization patches in the polar cap. *Journal of Geophysical Research*, *89*(A3), 1683–1694. https://doi.org/10.1029/JA089iA03p01683

Weber, E. J., Klobuchar, J. A., Buchau, J., Carlson, H. C. Jr., Livingston, R. C., de la Beaujardiere, O., et al. (1986). Polar cap f layer patches: Structure and dynamics. *Journal of Geophysical Research*, *91*(A11), 12121–12129. https://doi.org/10.1029/JA091iA11p12121

Winser, K., Jones, G., & Williams, P. J. S. (1986). A quantitative study of the high latitude ionospheric trough using eiscat's common programmes. *Journal of Atmospheric and Solar-Terrestrial Physics*, *48*(9–10), 893–904. https://doi.org/10.1016/0021-9169(86)90064-4

Zhang, Y., & Paxton, L. J. (2021). Storm-time neutral composition changes in the upper atmosphere. In *Upper atmosphere dynamics and energetics* (pp. 115–133). American Geophysical Union (AGU). https://doi.org/10.1002/9781119815631.ch7

Zhang, Y., Paxton, L. J., Morrison, D., Wolven, B., Kil, H., Meng, C.-I., et al. (2004). O/N_2 changes during 1–4 October 2002 storms: Image si-13 and timed/guvi observations. *Journal of Geophysical Research*, *109*(A10). https://doi.org/10.1029/2004JA010441

Zou, S., Perry, G. W., & Foster, J. C. (2021). Recent advances in polar cap density structure research. In *Ionosphere dynamics and applications* (pp. 67–82). American Geophysical Union (AGU). https://doi.org/10.1002/9781119815617.ch4

Zou, S., Ren, J., Wang, Z., Sun, H., & Chen, Y. (2021). Impact of storm-enhanced density (SED) on ion upflow fluxes during geomagnetic storm. *Frontiers in Astronomy and Space Sciences*, *8*, 746429. https://doi.org/10.3389/fspas.2021.746429